



TECHNISCHE
UNIVERSITÄT
WIEN
Vienna University of Technology

Diplomarbeit

A Search for Supersymmetry Using the Transverse Mass of the W Boson

Ausgeführt am
Institut für Hochenergiephysik (HEPHY)

Unter der Anleitung von
Univ. Prof. Dr. Christian Fabjan
und
Dr. Robert Schöfbeck

Durch
Stefan Kupstaitis-Dunkler

Obergrünbach 53
3822 Karlstein

Ort, Datum

Unterschrift

Abstract

This thesis has been done within the CMS data analysis group of the Institute for High Energy Physics, Vienna (HEPHY). It describes the search for new physics using data of proton-proton collisions at $\sqrt{s} = 8$ TeV recorded by the Compact Muon Solenoid (CMS) experiment at the Large Hadron Collider (LHC) located at the European Centre of Nuclear Research (CERN) in Geneva. The technical details of the LHC and its experiments are described, as well as the specifications of the CMS experiment. New physics, namely supersymmetrical particles, are interpreted within the concept of simplified models in the phenomenological Minimal Supersymmetric Standard Model (pMSSM). The pMSSM and its simplified model spectrum (SMS) is characterized.

The standard model (SM) background is discriminated from the expected signal using kinematic variables, such as the transverse mass of the W boson. A prediction of the transverse mass distribution is described in detail for the most important contributions to the SM background. Its most important systematic uncertainties are obtained, as well as a Maximum Likelihood fit of the prediction on data is performed. As a result, no evidence of new physics has been found, but upper limits on the cross sections for the involved new particles defined by the utilized SMS topologies are calculated and are presented.

Kurzfassung

Diese Arbeit wurde in der CMS-Datenanalysegruppe des Instituts für Hochenergiephysik (HEPHY) in Wien durchgeführt. Sie beschreibt die Suche nach neuer Physik unter Verwendung von Daten von Proton-Proton Kollisionen einer Schwerpunktsenergie von $\sqrt{s} = 8 \text{ TeV}$, die vom Compact Muon Solenoid (CMS) Detektor des Large Hadrons Colliders (LHC) aufgezeichnet wurden, der sich am Europäischen Kernforschungszentrum (CERN) in Genf befindet. Die technischen Details des LHC und dessen Experimente, sowie der CMS-Detektor werden beschrieben. Neue Physik, nämlich supersymmetrische Elementarteilchen, wird mit dem Konzept der “simplified models” im phenomenologischen minimalen supersymmetrischen Standardmodell (pMSSM) interpretiert. Das pMSSM und dessen simplified-model-Spektrum (SMS) wird charakterisiert.

Der Standardmodell-Hintergrund (SM) wird mit kinematischen Variablen, wie der transversen Masse des W-Bosons, vom erwarteten Signal unterschieden. Eine Vorhersage der Verteilungsfunktion dieser Variable für die wichtigsten Beiträge zum SM-Hintergrund wird detailliert beschrieben. Dessen wichtigste systematischen Unsicherheiten werden berechnet, sowie eine Maximum Likelihood Anpassung der Vorhersage an die Daten durchgeführt. Hinweise auf neue Physik sind nicht gefunden worden, aber obere Limits für die Produktionswirkungsquerschnitte der involvierten neuen Teilchen, die in den verwendeten SMS-Topologien definiert sind, werden berechnet und in dieser Arbeit präsentiert.

Danksagungen

Auf meinem Weg von meiner Geburt bis zum Fertigstellen der Diplomarbeit bin ich vielen Leuten begegnet, die dazu beigetragen haben, dass genau dieses Werk in dieser Form existieren kann. Zuerst möchte ich meinen Eltern, Leopold und Brigitte Dunkler, ganz herzlich danken, die mich unter höchsten Anstrengungen durchs Leben geführt haben, in einer Form, in der es mir scheinbar mühelos möglich war mein Studium zu absolvieren. Vielen Dank euch beiden! Desweiteren möchte ich mich auch bei meiner Zwillingsschwester Sandra für die Erwähnung meiner Wenigkeit in ihrer Diplomarbeit bedanken.

Meiner Gymnasiallehrerin, Marianne Schneider, die den Mathematik- und Physikunterricht immer sinnvoll und informationsgeballt gestaltet hat, gebührt deshalb besonderer Dank, weil sie mich gut auf das Physikstudium an der TU Wien vorbereitet hat. Dank geht auch an Herrn Prof. Dr. Christian Fabjan, der mit seiner offenen Art auf Studenten zuzugehen und seiner mehr als deutlich sichtbaren Begeisterung für Teilchenphysik, mein Interesse für eben diese geweckt hat und letztendlich auch der Grund war, warum ich meine Masterarbeit am HEPHY gemacht habe, nachdem ich im Jahr davor schon einmal im Zuge einer Projektarbeit in die Arbeit der CMS-Datenanalysegruppe des HEPHY schnuppern durfte. Robert Schöffbeck, meinem Betreuer, gebührt Dank, weil er jederzeit sehr bemüht war, das Niveau hoch zu halten und trotz der häufig komplizierten Sachverhalte nicht aufgegeben hat Dinge öfter als einmal zu erklären.

Weiteren Dank an:

- Janos Kancsar und Wolfgang Waltenberger, die sich während der Zeit am HEPHY ein Zimmer mit mir geteilt haben und auch Gespräche teilten, die abseits der Teilchenphysik führten, deren “Nerd-Faktor” aber nicht weniger gering war.
- Wolfgang Kiesenhofer, der manchmal Probleme im Vorbeigehen (zur Kaffeeküche) gelöst hat, von denen man vorher gar nicht gewusst hat, dass man sie hat.

Zu guter Letzt gilt mein Dank meiner Frau Milena, die ganz besonders mit dieser Arbeit verbunden ist, weil unsere Hochzeit während der Zeit, die ich am HEPHY verbracht habe, stattgefunden hat. Ihr möchte ich für die vielen schönen Stunden danken, die wir gemeinsam abseits der Physik verbracht haben.

The most merciful thing in the world, I think, is the inability of the human mind to correlate all its contents.

H. P. LOVECRAFT, "The Call of Cthulhu"

Contents

Abstract	iii
Danksagungen	vii
1. Theory	1
1.1. The Standard Model of Particle Physics	1
1.2. Deficiencies of the Standard Model	2
1.2.1. The Hierarchy Problem	3
1.3. Supersymmetry	4
1.3.1. The Minimal Supersymmetric Standard Model	5
1.3.2. Breaking Supersymmetry Softly	5
1.3.3. R-parity	6
1.3.4. The Phenomenological Minimal Supersymmetrical Standard Model	6
1.3.5. Simplified Models	7
2. The Large Hadron Collider	9
2.1. Technical Overview	9
2.2. The LHC Experiments	11
3. The Compact Muon Solenoid	13
3.1. Technical Overview	13
3.2. Superconducting Magnet	13
3.3. Inner Tracking System	14
3.4. Electromagnetic Calorimeter	14
3.5. Hadron Calorimeter	15
3.6. The Muon System	15
3.7. Trigger	16
3.7.1. The Level-1 Trigger	16
3.7.2. The High-Level Trigger	16
3.8. Event Reconstruction Process	17

4. Search in the Single Lepton Channel	19
4.1. Kinematic Variables	19
4.1.1. Missing Transverse Energy	19
4.1.2. Hadronic Activity	20
4.1.3. Identification of Bottom Quarks	20
4.1.4. Transverse Mass	22
4.2. Monte Carlo Simulation	22
4.3. SM Backgrounds	23
4.3.1. The $t\bar{t}$ Background	23
4.4. Event Selection	25
4.4.1. Muons	26
4.4.2. Electrons	26
4.4.3. Single Lepton Channel	27
4.5. QCD Background Yield Estimation	28
5. Prediction of the Transverse Mass Distribution	33
5.1. The Transverse Mass of the W Boson	33
5.2. Contributions to the Transverse Mass Shape	35
5.3. Prediction of the Transverse Mass Distribution Using Correction Templates	38
5.4. Single Lepton Prediction of the Transverse Mass Distribution from Dilepton Events	40
5.4.1. The $\tau \rightarrow \text{Hadrons} Lepton$ contribution	41
5.4.2. The $Lepton Lepton$ Contribution	44
5.5. Systematic Uncertainties on the Predictions	46
5.6. MC Simulation Prediction Correction Factors	47
6. Results	51
6.1. Maximum Likelihood Fit	51
6.1.1. Signal Binning	52
6.1.2. The Fit Model	52
6.1.3. The Likelihood Function	53
6.1.4. Fit Results	54
6.2. Limit Calculation	58
6.2.1. Observed Limit	58
6.2.2. Expected Limit	59
6.2.3. Resulting Exclusion Limits	59
7. Summary and Outlook	65

Appendices

Appendix A. Datasets and Tables	69
A.1. Dataset Used for QCD Estimation	69
A.2. Dataset Used for Dilepton Prediction	69
Appendix B. Programs and Tools	71
B.1. Higgs Combine Tool	71
List of Tables	74
List of Figures	76
Bibliography	79

1. Theory

1.1. The Standard Model of Particle Physics

The Standard Model of particle physics (SM) is a theory, which describes the interactions of the elementary particles, as well as three out of four fundamental forces, the electromagnetic force, the weak force and the strong force based on quantum field theory [1, 2]. It was completed by the discovery of the Higgs boson in 2012.

Elementary particles can be grouped into fermions and bosons. Leptons and quarks are fermions and they can be further classified in three families, whose members are listed in Tab. 1.1. Each of the fundamental interactions is mediated by the exchange of virtual bosons. The electromagnetic interaction between a pair of electrically charged particles is mediated by the exchange of photons. The weak interaction is mediated by the exchange of the Z boson or the electrically charged W^+/W^- bosons. The strong interaction between color charged particles is mediated by the exchange of gluons. The electromagnetic and weak interactions are unified in the so-called electroweak theory.

Table 1.1.: Particle content of the SM

	first generation	second generation	third generation
quarks	up, down	charm, strange	top, bottom
leptons	e, ν_e	μ, ν_μ	τ, ν_τ
bosons	photon, W and Z, gluons		
	Higgs boson		

Quarks are subject to the quark confinement phenomenon, which entails that a single quark cannot be observed. Quarks always form hadrons, which can consist of a quark and an anti-quark (mesons) or of three quarks (baryons). In order to fulfill the Pauli exclusion principle for the baryon constituents, a color “charge” is introduced guaranteeing the wave function to be antisymmetric at all times. The labels of the colors are red, blue or green, anti-quarks carry the respective anti-colors. Gluons, as the mediators of the strong force, carry color and anti-color described by an eight-dimensional representation of $SU(3)$. Observable particles are always color neutral.

Another important part of the SM is the Cabibbo–Kobayashi–Maskawa (CKM) matrix describing the mechanism of quark flavor change due to the weak interaction [1]. The matrix encodes the transitions of quarks from one generation into quarks from another generation. It is also responsible for the CP-violation in weak decays.

The Lagrangian of the SM depends on 19 empirical parameters, including the masses of the elementary particles, the CKM mixing angles, the CP-violating phase and the gauge coupling constants. It is invariant under transformations of the local gauge group $SU_C(3) \times SU_L(2) \times U_Y(1)$. By means of spontaneous symmetry breaking of the electroweak Lagrangian, the SM fermions and the W and Z bosons acquire mass, while the photon is left massless.

1.2. Deficiencies of the Standard Model

Despite the fact the SM is a well tested theory, there are pertinent questions, the SM cannot answer:

Measurements of galactical dynamics from 1933 could not be explained by visible matter [3]. Therefore, a new type of so-called dark matter was introduced, that is required to interact at most only weakly. There are many competing dark matter candidate theories, some of which explain dark matter as weakly interacting massive particles (WIMP). In Sec. 1.3.3, one of these WIMP candidates is motivated by supersymmetrical models being able to predict a WIMP like dark matter candidate. Dark energy is a hypothetical form of energy interacting only gravitationally, that is used to explain the apparent acceleration of the expansion of the universe [4]. Today, we estimate that the energy content of the universe is composed of about 4.9% of ordinary matter described by the SM, roughly 26.8% dark matter and 68.3% dark energy.

After the unification of the electromagnetic and the weak interactions, many attempts of including the strong interactions in a “Grand Unified Theory” (GUT) have been made [5,6]. Their coupling constants are energy dependent and in GUT theories, they merge at high energies. In Fig. 1.1, it can be seen, that the continuation of the strength of the coupling constants to high energies in the SM does not converge for all three interactions.

Another even more difficult goal is the unification of a theory of gravitation with the SM. A postulated, not yet found particle, the carrier of the fourth, gravitational force,

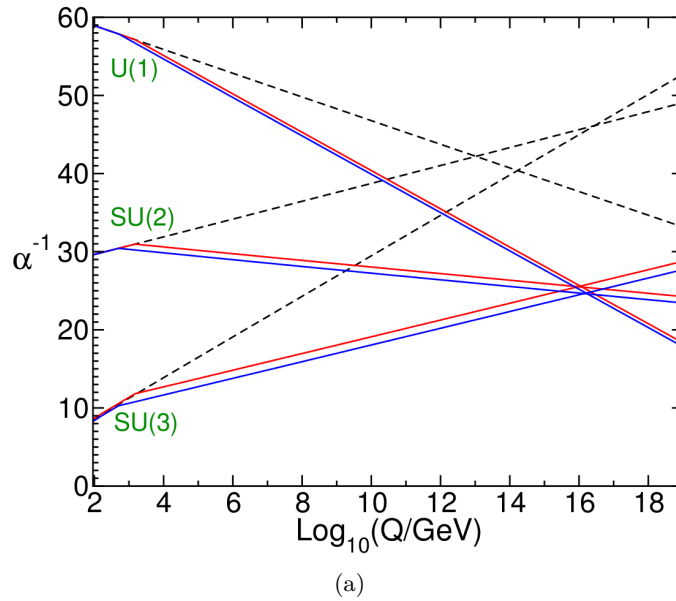


Figure 1.1.: Running of the inverse coupling constants for the three interactions as a function of energy for SM only physics (dashed lines). In Sec. 1.3 the minimal supersymmetric standard model is introduced in which the coupling constants are unified at the GUT scale (solid lines) [7].

is the Graviton.

1.2.1. The Hierarchy Problem

The so-called *hierarchy problem* arises from the quantum loop corrections to the mass of the Higgs boson [7]. The problem is that the Higgs boson mass receives enormous quantum corrections from the virtual effects of every particle that couples, directly or indirectly, to the Higgs field. Due to the commuting and anticommutating nature of bosons and fermions, respectively, the correction for bosons and fermions have opposite signs. A loop containing a fermion f of mass m_f , which couples to the Higgs field H with a term $-\lambda_f H \bar{f} f$ in the Lagrangian density, as depicted in Fig. 1.2 (a), results in a correction

$$\Delta m_H^2 = -\frac{|\lambda_f|^2}{8\pi^2} \Lambda_{UV}^2 + \dots, \quad (1.1)$$

where λ_f is the coupling of the fermion to the Higgs field, and Λ_{UV} is the ultraviolet momentum cutoff, representing the energy scale of new physics entering to change the high-energy physics behavior of the theory. Both, leptons and quarks, couple to the

Higgs field as described in Eq. (1.1). The biggest correction comes from the top quark, where $\lambda_f \approx 1$.

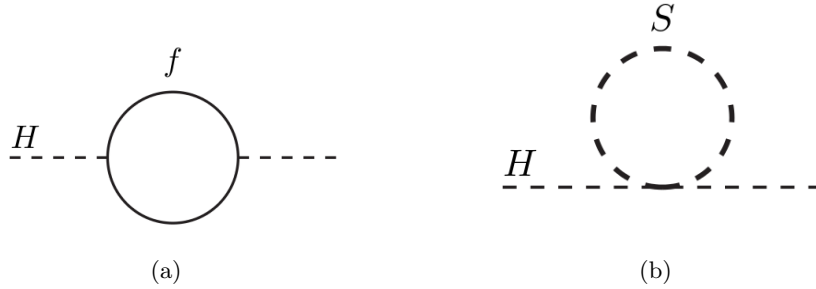


Figure 1.2.: (a) Fermion f coupling to a Higgs boson and (b) scalar coupling to a Higgs boson.

The scalar particle S with mass m_S in Fig. 1.2 (b) yields a correction

$$\Delta m_H^2 = \frac{\lambda_s}{16\pi^2} \left[\Lambda_{UV}^2 - 2m_S^2 \ln(\Lambda_{UV}/m_S) + \dots \right]. \quad (1.2)$$

The term proportional to Λ_{UV}^2 cannot be canceled without a physically unjustifiable tuning of a counter-term. It is a problem of the SM, that the mass of the Higgs boson is so small, when it is sensitive to particles with the highest masses, such as the top quark.

1.3. Supersymmetry

Supersymmetry (SUSY) is a symmetry transformation, which is capable of solving the hierarchy problem, described in the previous section. A SUSY transformation turns a bosonic state into a fermionic state and a fermionic state into a bosonic state. Thus, extending the SM with SUSY, each particle has a so-called superpartner. Every fermion has a bosonic partner named by putting “s” in front of the fermion’s name and every boson has a fermionic partner named by putting ‘ino’ after the boson’s name. Therefore, for each fermion that couples to the Higgs boson, and thus contributes to the Higgs boson mass, there is a bosonic counter-term that systematically cancels the fermionic contributions, and vice versa.

1.3.1. The Minimal Supersymmetric Standard Model

The Minimal Supersymmetric Standard Model (MSSM) is a supersymmetric extension of the SM with minimal particle content. It introduces spin-0 superpartners of the spin-1/2 quarks and leptons, the squarks and sleptons. Moreover, two chiral superfields are introduced containing the Higgs bosons of spin 0 and their superpartners, the spin-1/2 Higgsinos. The spin-1 gauge bosons and their spin-1/2 superpartners are arranged in vector supermultiplets. The MSSM is based on the SM gauge symmetry $SU_C(3) \times SU_L(2) \times U_Y(1)$ [8]. A list of particles of the MSSM can be found in Tab. 1.2

Table 1.2.: Particles and their superpartners in the unbroken MSSM

Fermions	Bosons
Quarks: u, d, s, c, t, b	Squarks: $\tilde{u}, \tilde{d}, \tilde{s}, \tilde{c}, \tilde{t}, \tilde{b}$
Leptons: $e, \mu, \tau, \nu_e, \nu_\mu, \nu_\tau$	Sleptons: $\tilde{e}, \tilde{\mu}, \tilde{\tau}, \tilde{\nu}_e, \tilde{\nu}_\mu, \tilde{\nu}_\tau$
Gluino: \tilde{g}	Gluon: g
Wino, Zino: \tilde{W}, \tilde{Z}	W, Z
Photino: $\tilde{\gamma}$	Photon: γ
Higgsinos: \tilde{H}	Higgs bosons: H

1.3.2. Breaking Supersymmetry Softly

If supersymmetry were an unbroken symmetry, superpartners would have the same mass as the corresponding SM particles. Since none of the superpartners have been found yet, supersymmetry is considered to be broken. Constraints on the nature of supersymmetry breaking can be obtained from the hierarchy problem. In unbroken supersymmetry, the loop corrections from SM fermions to the Higgs mass cancel the bosonic loops. Thus, it is necessary to maintain the relation of the associated dimensionless couplings. Therefore, the concept of “soft” supersymmetry breaking is introduced by adding “soft” terms to the Lagrangian of the MSSM in the form

$$\mathcal{L} = \mathcal{L}_{SUSY} + \mathcal{L}_{soft}, \quad (1.3)$$

where \mathcal{L}_{SUSY} conserves supersymmetry, and \mathcal{L}_{soft} , violates supersymmetry, but does not spoil the cancellation of the loop corrections to the Higgs self energy. The mass terms m_{soft} contribute with corrections to the Higgs mass in the form

$$\Delta m_H^2 = m_{soft}^2 \left[\frac{\lambda}{16\pi^2} \ln(\Lambda_{UV}/m_{soft} + \dots) \right]. \quad (1.4)$$

Since these mass terms, which determine the mass splittings between the known SM particles and their superpartners, are logarithmically dependent on Λ_{UV} , they cannot be too large, in order not to lose the successful handle of the hierarchy problem. An estimation results in the TeV scale as upper mass limits for the lightest superpartners.

While \mathcal{L}_{SUSY} thus derives from the SM, the supersymmetry-breaking terms introduce a large number of mixing angles and CP-violating phases.

1.3.3. R-parity

In the MSSM the general superpotential for the construction of the Lagrangian contains terms which violate the lepton (L) and the baryon number (B). Since this allows the proton to decay within the fraction of a second in the general case, a new symmetry is introduced, in order to eliminate B and L violating terms from the superpotential. This new symmetry is called R-parity, or matter parity. For each particle in the theory carrying spin s , R-parity is a multiplicatively conserved quantum number defined as

$$P_R = (-1)^{3(B-L)+2s}. \quad (1.5)$$

All Standard Model particles and the Higgs bosons carry $P_R = +1$, while squarks, sleptons, gauginos and higgsinos have an R-parity $P_R = -1$. A term in the Lagrangian density is allowed, if the product of all P_R is $+1$. Thus, all the B and L violating terms in the general superpotential of the MSSM are forbidden.

If R-parity is exactly conserved, there can be no mixing between particles and sparticles, and every vertex must contain an even number of sparticles. Therefore, the lightest supersymmetric particle (LSP) must be stable. If it is electrically neutral, it interacts only weakly with ordinary matter and thus, it is an interesting candidate for a source of non-baryonic dark matter, the so-called weakly interacting massive particles (WIMPs).

1.3.4. The Phenomenological Minimal Supersymmetrical Standard Model

The unconstrained MSSM has a huge number of free parameters arising from the softly supersymmetry breaking part of the Lagrangian density, introducing 105 new parameters, in addition to the 19 SM parameters [8]. In order to retain predictive power, the number of parameters is reduced. Several phenomenological constraints lead to

assumptions that constrain the MSSM.

First, as no experimental evidence has been found justifying CP-violating terms in the Lagrangian density, CP-violating terms are eliminated. Secondly, experimental data constrains violations of flavor changing neutral currents which simplifies the sfermion mass matrices, and therefore means a reduction of parameters. Due to experimental evidence, the mass splitting of the first and second generation squarks is highly limited. Thus, the last constraint is made by assuming the masses of the first and second generations of sfermions are the same, and by setting the Yukawa couplings of the first two generations zero. After applying these constraints, 19 input parameters are remaining in the so-called phenomenological MSSM (pMSSM).

1.3.5. Simplified Models

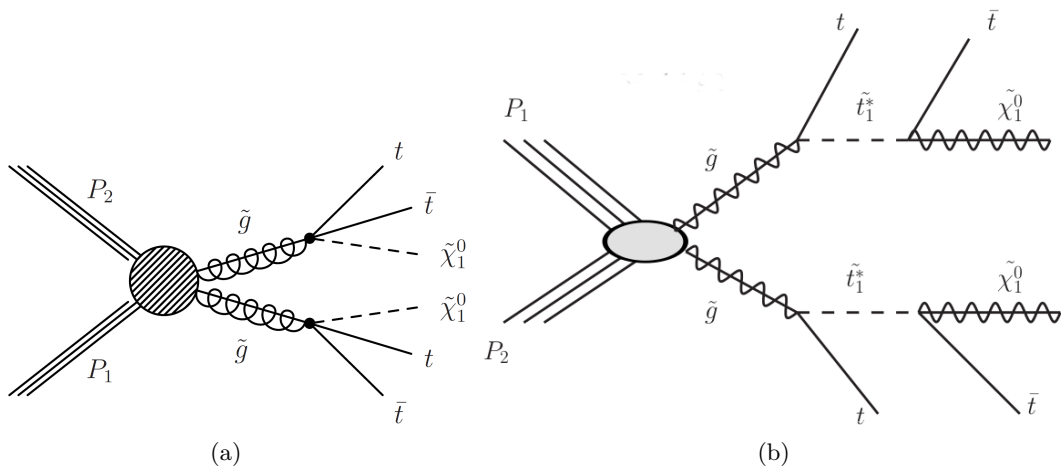


Figure 1.3.: Both figures show the Feynman diagrams of the same decays for different simplified models. (a) shows the decoupled stop scenario, where the stop mass is fixed at a high value. (b) shows the Feynman diagram for the frozen neutralino mass scenario and the frozen gluino mass scenario.

Because of the hierarchy problem discussed earlier, and because of naturalness, which states, that the parameters in a theory should be of the same order, the mass of the partner of the top quark is required not to be much higher than the top quark mass scale. This is implemented in the models considered, which is done by utilizing the so-called simplified models for purposes of interpretation within this thesis.

The framework of simplified models is designed to involve only a few new particles

and interactions [9]. Many of them are limits of more general physics scenarios, which involve more particles than the corresponding simplified model. They can be well described with only a small number of parameters relevant in collider experiments, such as the particle masses, production cross-sections and branching ratios. In this thesis, the selection of models is motivated by the particles and interactions of the MSSM. The primary applications of simplified models are:

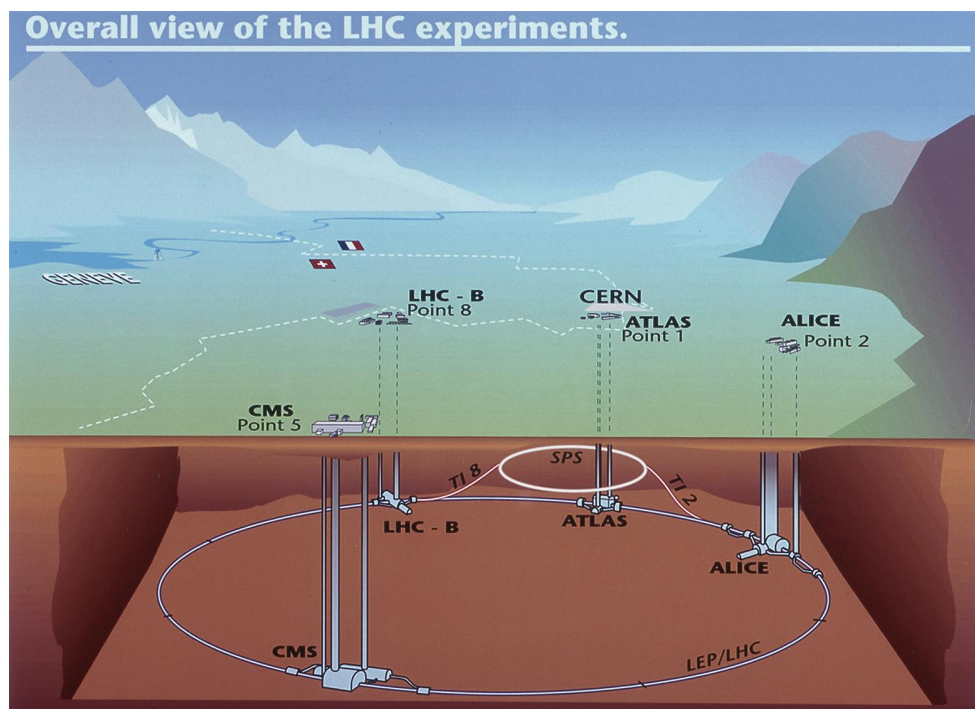
- Determining the limits of search sensitivity.
- Discovering new physics signals.
- Obtaining constraints on more general models of the underlying theory.

The three simplified models used within this thesis, are restricted to interactions of these three sparticles: the gluino, the stop quark and the neutralino in the role of the LSP according to the underlying pMSSM. In a proton-proton collision a gluino pair is produced, that decays into two stop and two top quarks. Each of the stop quarks further decays into a neutralino and an top anti-quark. Since the neutralino is stable and only interacts weakly with other particles, it leaves the detector unseen resulting in missing energy. Missing energy and a high hadronic activity are typical signatures for this SMS.

In each of the three models the mass of one of the sparticles is constrained, while the other two particle masses define a parameter plane. The first model spans a parameter plane using the neutralino mass and the gluino mass and is shown in the Feynman diagram in Fig. 1.3 (a). In fact, in this model, the stop quark mass does not matter provided that it is much bigger than the difference of the gluino and the top quark mass. Henceforth, it is called the “decoupled stop scenario”. The so-called “frozen neutralino mass scenario” utilizes the mass of the gluino and the stop quark, while keeping the LSP mass constant and can be viewed in Fig. 1.3 (b). The model, where the gluino mass is held constant is referred to as the “frozen gluino mass scenario” within this thesis and the Feynman diagram is the same as for the frozen neutralino mass scenario.

2. The Large Hadron Collider

2.1. Technical Overview



(a)

Figure 2.1.: A scheme of the LHC accelerator complex with an overall view of the experiments [10]

The Large Hadron Collider (LHC) is a two-ring, superconducting accelerator and collider installed in a 27 km long tunnel, previously used for the LEP collider. The LHC physics program aims at the discovery of new physics and the study of rare events in proton-proton and ion-ion collisions. In p-p collisions with center of mass collision energies of up to 14 TeV correspond to a nominal energy of 7 TeV for each beam [11]. In the first runs the LHC was operated at 7 (2011) and 8 TeV (2012).

The number of events per second (N) is given by:

$$N = L\sigma, \tag{2.1}$$

where L is the LHC instantaneous luminosity and σ is the cross section of the process under consideration. The cross section is measured in barns. One barn (b) corresponds to 10^{-24} cm². The luminosity is measured in inverse barns (b⁻¹). The luminosity can be calculated from the beam parameters as

$$L = \frac{N_b^2 n_b f \gamma}{4\pi \epsilon_n \beta^*} F, \tag{2.2}$$

where N_b is the number of particles per bunch, n_b the number of bunches per beam, f the revolution frequency, γ the relativistic gamma factor, ϵ_n the normalized transverse beam emittance, β^* the beta function at the collision point, and F the geometric luminosity reduction factor due to the crossing angle at the interaction point.

The colliding objects in high energy proton-proton collisions are the constituents of the protons (partons): its valence quarks, gluons and sea quarks [12]. At a center of mass energy of 8 TeV, the TOTEM experiment at the LHC measured the total cross section to be $\sigma_{p-p} = 101.7 \pm 2.9$ mb in 2012 [12] [13]. With the luminosity integrated over time in the year 2012, $\mathcal{L} = 20$ fb⁻¹, we calculate roughly 10^{15} collisions. The theoretical cross section for a gluino pair arising in a 8 TeV p-p collision for a gluino of mass 800 GeV is ≈ 0.15 pb, while QCD background events appear with a cross section in the scale of mbarns. Thus, in the whole year 2012, only approximately thousands of potential signal events would be produced.

The design peak luminosity of the two high luminosity experiments the Compact Muon Solenoid (CMS) [14] and A Toroidal LHC Apparatus (ATLAS) [15] is $L = 10^{34}$ cm⁻²s⁻¹. Two rings with opposite magnetic dipole fields are needed for colliding protons with protons. Therefore, each of the proton beams requires a separate vacuum chamber. For technical and economic reasons, the LHC uses twin bore magnets that consist of two sets of coils and beam channels within the same mechanical structure and cryostat. The maximal beam energy depends on the integrated dipole field in the storage ring, where a peak dipole field of 8.33 T allows to accelerate protons to up to 7 TeV. The LHC magnets use NbTi cables and are cooled to a temperature below 2 K using superfluid helium.

In order to accelerate the protons to up to 7 TeV several pre-accelerators are used

before the protons are injected into the LHC. The injected beams are captured, accelerated and stored using a 400 MHz superconducting cavity system, before they are brought to collision at the various interaction points of the experiments. An overview of the experiments and the Super Proton Synchrotron (SPS) pre-accelerator, which accelerates the protons to up to 450 GeV before they are injected in the LHC, is given in Fig. 2.1.

2.2. The LHC Experiments

- **A Large Ion Collider Experiment (ALICE)**
ALICE is a general-purpose, heavy-ion detector focussing on the strong interactions within the Standard Model. It was designed to study new physics of strongly interacting matter and the quark-gluon plasma at extreme values of energy density and temperature. High densities of energy and temperature are reached with heavy-ion collision, e.g., Pb-Pb. The proton-proton runs at the LHC provide reference data for the heavy-ion program [16].
- **Compact Muon Solenoid (CMS) and A Torroidal LHC Apparatus (ATLAS)**
Two general purpose detectors, ATLAS and CMS, are designed for probing p-p and ion-ion collisions at a high value of luminosity, in order to discover processes with a low production cross section. Their program is to make high precision measurements of SM quantities, discovering new physics, such as supersymmetrical particles, of which one might be a candidate for dark matter, and extra dimensions. An accomplished goal of these experiments was the discovery of the Higgs boson. A more detailed description of the CMS experiment follows in Sec. 3 [15].
- **LHCb**
The amount of anti-matter in the universe cannot be explained by CP violating processes of the electroweak interaction. Therefore the LHCb experiment's primary goal is to search for new physics in CP violating processes and rare decays of beauty and charm hadrons [17].
- **LHCf**
The LHCf is an experiment performing a measurement of the very forward production cross sections and energy spectra of neutral pions and neutrons, in order to compare and calibrate experiments using cosmic rays [18].
- **TOTEM**
The goal of TOTEM is a measurement of the total proton-proton cross-section

using a luminosity-independent method and a deeper understanding of the proton structure [13].

3. The Compact Muon Solenoid

3.1. Technical Overview

The central feature of the Compact Muon Solenoid (CMS) apparatus is a superconducting solenoid of 6 m internal diameter, providing a magnetic field of 3.8 T [14]. The overall dimensions of the CMS detector are a length of 21.6 m, a diameter of 14.6 m and a total weight of 12500 tons. Within the volume of the superconducting solenoid, there are a silicon pixel and strip tracker, a lead tungstate crystal electromagnetic calorimeter (ECAL), and a brass/scintillator hadron calorimeter (HCAL). Muons are measured in gas-ionization detectors embedded in the steel return yoke outside the solenoid. Extensive forward calorimetry complements the coverage provided by the barrel and endcap detectors.

CMS uses a right-handed coordinate system, with the origin at the nominal interaction point, the x axis pointing to the centre of the LHC, the y axis pointing up (perpendicular to the LHC plane), and the z axis along the counterclockwise-beam direction. The azimuthal angle ϕ is measured in the transverse ($x - y$) plane from the x axis. The polar angle θ is measured from the positive z axis and the pseudorapidity η is given by

$$\eta = -\ln \tan(\theta/2). \quad (3.1)$$

Fig. 3.1 shows a cross section of the CMS apparatus.

3.2. Superconducting Magnet

Since magnetic fields bend the trajectories of charged particles, they provide the basis to measure the particles momentum. In order to reach the desired magnetic field, the magnet is required to be superconducting. The solenoid has a free bore of 6 m diameter and 12.5 m length. In the solenoid's magnetic field, an energy of 2.6 GJ is stored at maximal current.

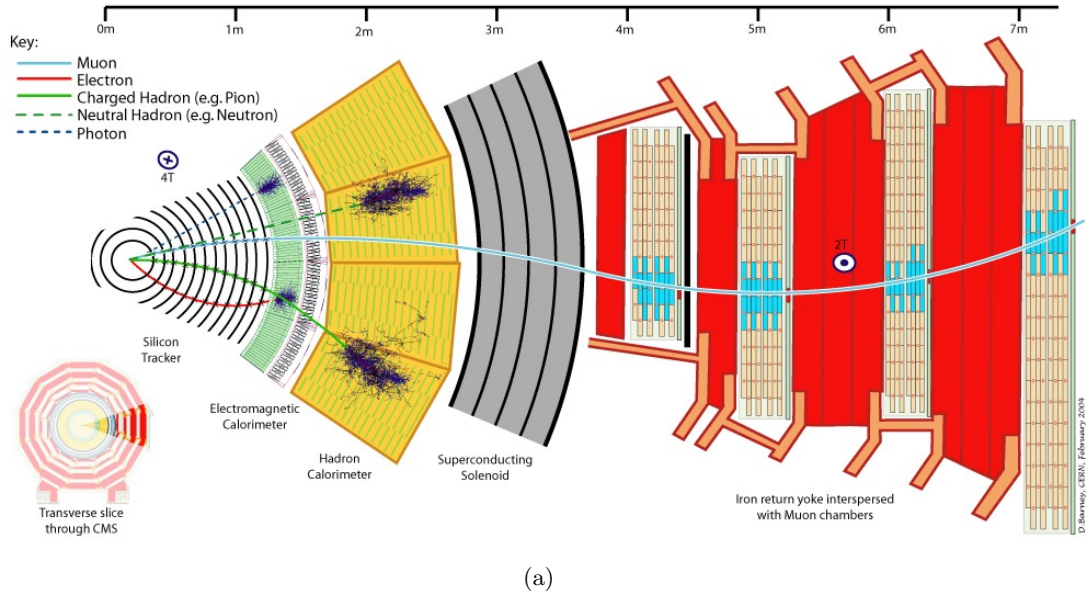


Figure 3.1.: The Compact Muon Solenoid. A view of the transverse plane [19].

3.3. Inner Tracking System

The inner tracking system is built to deliver a precise and efficient measurement of the trajectories of charged particles, along with a precise reconstruction of secondary vertices. It is 5.8 m long and has a diameter of 2.5 m. Because of more than 1000 particles produced per bunch crossing, a fast response and high granularity are required under the condition of using a minimum amount of material. This led to the choice of silicon detector technology, which has to be also radiation resistant. The inner tracking system is separated into a barrel part and two endcaps at each side of the barrel. The barrel is composed of 3 pixel layers up to a radius of 10.2 cm and 10 layers of silicon strips up to a radius of 1.1 m. The endcaps are composed of 2 disks of pixel detectors and 3 inner, as well as 9 outer disks of strip detectors. The endcaps extend the acceptance of the inner tracking system to $|\eta| < 2.5$.

3.4. Electromagnetic Calorimeter

The electromagnetic calorimeter (ECAL) barrel is made of 61200 lead tungstate (PbWO_4) crystals and each of the endcaps utilizes 7342 of them. The ECAL is fast, radiation resistant, of high granularity and has an excellent energy resolution. In front of the endcap crystals a preshower detector is placed. The photo detectors used in the barrel

are avalanche photo diodes, while the endcaps use vacuum phototriodes.

3.5. Hadron Calorimeter

The hadron calorimeter (HCAL) measures the hadronic component of jets. It consists of several parts: The barrel (HB) and endcaps (HE) are placed outside the ECAL at a radius $1.77 \text{ m} \leq R \leq 2.95 \text{ m}$ from the interaction point. The outer HCAL (HO) encloses the solenoid. The Cherenkov-based forward hadron calorimeters (HF) covers the range $3 \leq |\eta| \leq 5.2$ using radiation-hard technology. These parts of the HCAL are drawn in Fig. 3.2.

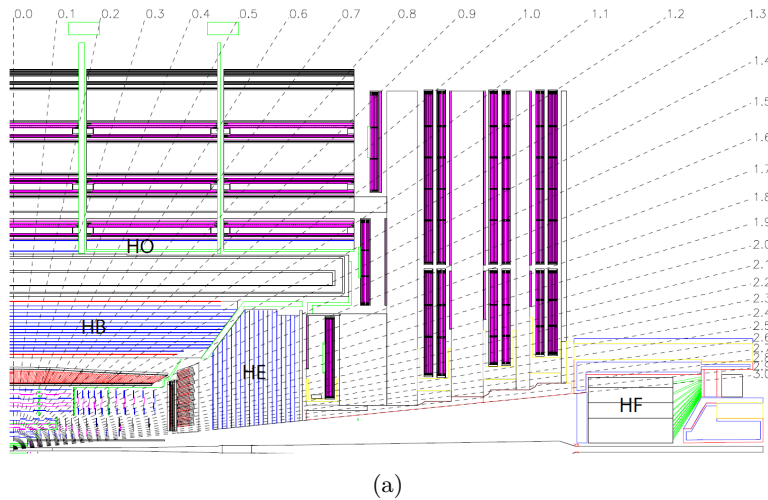


Figure 3.2.: Schematic view of the tracker, the ECAL, HCAL, HF, the magnet and the muon system [14].

3.6. The Muon System

The efficient detection of muons is a primary design goal of the CMS detector. The CMS muon system provides identification, momentum measurement and trigger capabilities. Three types of detectors are used to reach these goals. In the barrel region of $|\eta| < 1.2$, where the magnetic field is uniform, drift tube (DT) chambers are used, composed of 4 stations, which contain chambers used for the measurement of the muon coordinates in the r - ϕ plane, as well as in the z direction. In the two endcap regions $0.9 \leq |\eta| \leq 2.4$, where the muon rate is high and the magnetic field is non-uniform, cathode strip chambers (CSC) are used. As described in the following section, the DT and CSC select by the transverse momentum of muons with a good efficiency and a high background

rejection. They have a short response time, a fine segmentation and are radiation resistant. Complimentary to those two detector systems, several layers of resistive plate chambers are used. An alignment system measures the relative positions of the muon detectors to each other and to the inner tracker, in order to improve the spatial resolution of the reconstructed hits.

3.7. Trigger

Since it is impossible to store and process all the data produced by the LHC at its design luminosity, a trigger system reduces the rate in two steps, specifically the Level-1 (L1) Trigger and the High-Level Trigger (HLT). The requirement on both trigger systems are that the selection satisfies the conditions of the CMS physics program. Therefore, the efficiency of the physics objects must be as high as possible, whereas the triggered selection must be as inclusive as possible, since unexpected new phenomena may arise at the LHC energies. The combined reduction rate of the L1 Trigger and the HLT must be of an order of 10^6 . The L1 Trigger consists of programmable electronic systems, whereas the HLT is built of about 1000 commercial processors.

3.7.1. The Level-1 Trigger

The L1 Trigger consists of three parts, the Muon Trigger, the Calorimeter Trigger and the Global Trigger. The Muon Trigger and the Calorimeter Trigger have local, regional and global components. The local components of the Muon Trigger receive information from its detector subsystems, the DT, the CSC and the RPC, while the Calorimeter Trigger takes its information from the ECAL, HCAL and HF. In both systems, the regional components combine the information of their subsystems and determine rankings of the trigger objects, e.g., sorted lists of electron and muon candidates, and make links between the detector systems. Their global components, determine the highest-rank muon and calorimeter objects, respectively and transfer them to the Global Trigger at the top of the L1 Trigger hierarchy. The Global Trigger finally takes the decision, if an event is rejected or accepted for further evaluation by the HLT. The general architecture of these relations are depicted in Fig. 3.3.

3.7.2. The High-Level Trigger

The HLT has access to the data and processes all events accepted by the L1 Trigger [20]. The selection is optimized towards a fast rejection while minimizing the CPU usage at the same time. To this end a simplified online reconstruction is performed.

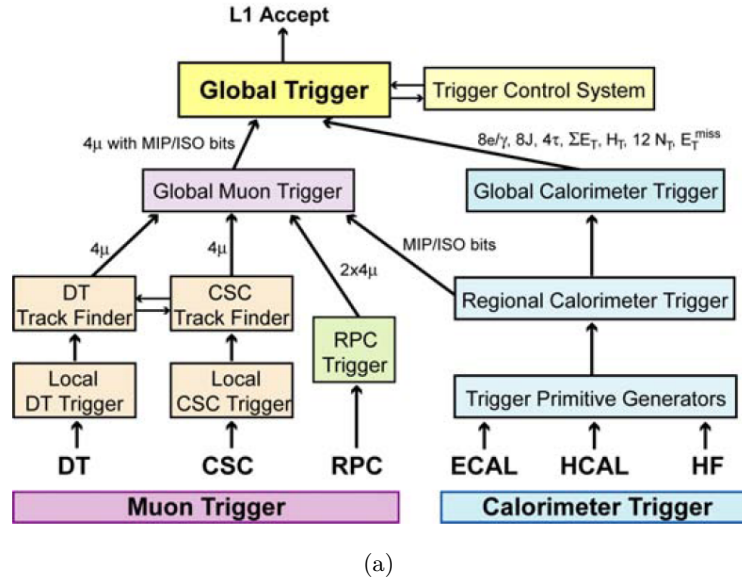


Figure 3.3.: Architecture of the L1-Trigger [14].

Electrons and photons are identified in three steps. First, only calorimeter information is utilized. Step two tests the candidate for an appropriate track with a certain number of hits in the pixel detector, followed by a match or a failure to match to the ECAL cluster, thereby distinguishing electrons and photons, respectively. The last step is the full track reconstruction.

Muon identification is based on two steps. The muon is first reconstructed in the muon chambers confirming the L1 decision and refining the p_T measurement. This is followed by an extension of the trajectories to the tracker.

3.8. Event Reconstruction Process

The event reconstruction is done by using the so called particle flow event reconstruction [21,22]. It consists in reconstructing and identifying each particle with a combination of all subdetector information. In this process, the particle type (photon, electron, muon, charged hadron, neutral hadron), as well as the particle momentum and energy are determined. Photons are identified as ECAL energy clusters which are not matched to the extrapolation of any charged particle trajectory to the ECAL. Electrons are identified as a primary charged particle track and potentially many ECAL energy clusters corresponding to this track extrapolation to the ECAL and to possible bremsstrahlung photons emitted along the way through the tracker material. Muons are identified as

a track in the central tracker consistent with either a track or several hits in the muon system, possibly associated with a low energy deposit in the calorimeters. Charged hadrons are identified as charged particle tracks neither identified as electrons, nor as muons. Finally, neutral hadrons are identified as HCAL energy clusters not linked to any charged hadron trajectory, or as HCAL energy excesses with respect to the expected charged hadron energy deposit.

The energy of photons is directly obtained from the ECAL measurement and corrected for zero-suppression effects. The energy of electrons is determined from a combination of the track momentum at the main interaction vertex, the corresponding ECAL cluster energy, and the energy sum of all bremsstrahlung photons attached to the track. The energy of muons is obtained from the corresponding global track momentum. The energy of charged hadrons is determined from a combination of the track momentum and the corresponding ECAL and HCAL energy, corrected for zero-suppression effects, and calibrated for the nonlinear response of the calorimeters. Finally, the energy of neutral hadrons is obtained from the corresponding calibrated HCAL energy.

For each event, hadronic jets are clustered from these reconstructed particles using the anti- k_t algorithm, which sequentially clusters all particles within a cone around the hardest jet [23]. Jet energy corrections are derived from the simulation, and are confirmed with local measurements with the energy balance of dijet and photon+jet events [24].

4. Search in the Single Lepton Channel

This section introduces the kinematic variables, as well as basic analysis tools such as Monte Carlo simulation methods used in a search for new physics. The selections for muons, electrons in the single lepton channel are explained, and a description of the main SM backgrounds corresponding to the applied selection of data is given. The data sets utilized for the search of new physics in the single lepton channel are specified. At the end of the section, an estimation of the QCD background is provided serving as an example of a data-driven background prediction method.

4.1. Kinematic Variables

The common signatures of the signal models described in Sec. 1.3.5 are quarks, decay products of the quarks (leptons) and non-detectable particles (neutralinos, neutrinos). These signal models motivate the introduction of a few kinematic variables able to discriminate between SM background and new physics.

4.1.1. Missing Transverse Energy

The colliding partons have negligible momenta in the transverse plane. According to the laws of conservation of momentum and energy, the sum of transverse momenta of the created particles ought to be equal the momentum of the system of incoming partons and thus, be small as well. Since the parton momentum along the beam axis is not known, only the transverse momentum imbalance (missing transverse energy) can be considered. The missing transverse energy, abbreviated \cancel{E}_T is defined as the negative vectorial sum of all transverse momenta of all final-state particles reconstructed in the detector:

$$\cancel{E}_T = - \sum_i \vec{p}_{T,i} \quad (4.1)$$

Particles, which escaped detection, along with mismeasurements in the calorimetric systems result in missing energy.

The \cancel{E}_T variable undergoes several corrections. Two important corrections are the jet energy correction and the ϕ correction. The first originates in the measurement of the jet energy in the calorimetric system. As the calorimeter response is not perfectly linear to the energy deposit of particles, jet energy corrections are applied in order to map the measured jet energy properly. These jet energy corrections are also taken into account for the calculation of the \cancel{E}_T . The second correction originates in the circumstance, that the distribution of \cancel{E}_T should be uniform in the xy -plane. However, the observed data shows a slight \cancel{E}_T sinusoidal dependence on ϕ , which can be caused by anisotropic detector responses, inactive calorimeter cells, the detector misalignment and the displacement of the beam spot. The amplitude of this sinusoidal dependence can be reduced by shifting the coordinate system in the transversal plane [25].

In events involving weak decays to charged leptons, high energetic neutrinos are produced, and a genuine \cancel{E}_T is expected. High \cancel{E}_T is also a SUSY signature, since neutralinos only interact weakly and are not detected. A \cancel{E}_T distribution is shown in Fig. 4.1 (a).

4.1.2. Hadronic Activity

Two frequently used measures of hadronic activity are the multiplicity of jets n_{jets} and the H_T variable. A reconstructed anti- k_T jet is considered if it passes the requirements $p_T > 40 \text{ GeV}$ and $|\eta| < 2.4$. The total *hadronic activity* (H_T) is defined as the scalar sum of the transverse jet momenta

$$H_T = \sum_{j=jets}^{n_{jets}} p_T^j. \quad (4.2)$$

Figure 4.1 (b) depicts an H_T distribution, while Fig. 4.1 (c) shows an n_{jets} distribution.

4.1.3. Identification of Bottom Quarks

Bottom quarks have a relatively long lifetime. The tagging of bottom quarks (b-tagging) is a process which “tags” a jet as originating from a b quark. If there is a secondary vertex in the event, it is used along with variables associated with this vertex, e.g., flight distance and direction, to discriminate between b jets and other jets. The Combined Secondary Vertex (CSV) is based on the combination of the secondary vertex variables together with track-based lifetime information. A quark is tagged if it is below the discriminator value of the CSV medium working point [26]. A b-tagged jet increases the n_{btags} variable in an event by one. Figure 4.1 (d) shows an n_{btags} distribution.

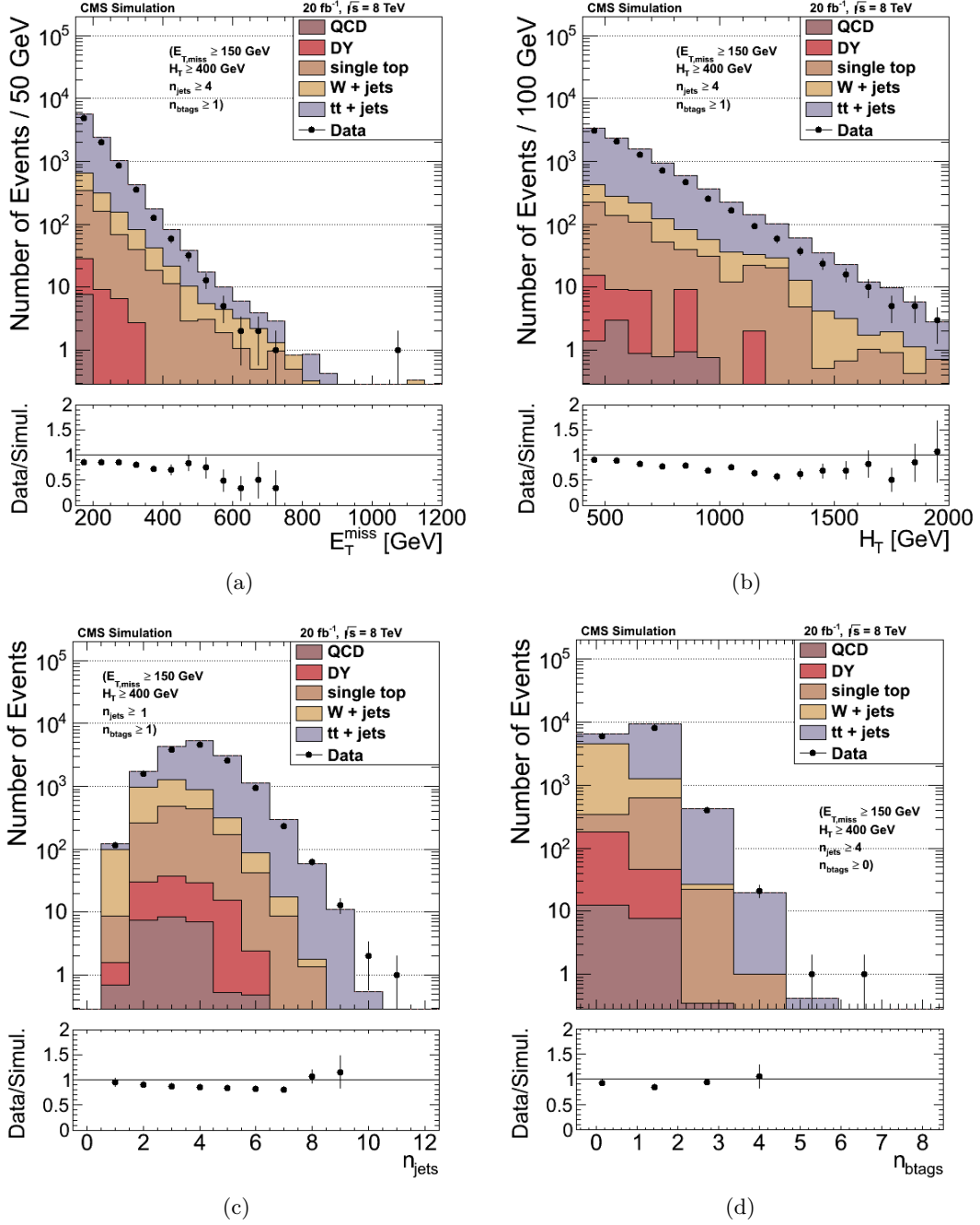


Figure 4.1.: Distributions for single lepton preselection, showing observed data compared to standard model backgrounds obtained from simulations. E_T (a) and H_T (b) distributions for a single lepton preselection $E_T \geq 150 \text{ GeV}$, $H_T \geq 400 \text{ GeV}$, $n_{\text{jets}} \geq 4$, $n_{\text{btags}} \geq 1$, showing observed data compared to the standard model backgrounds obtained from simulations. Both distributions show an approximately exponential decrease. (c) n_{jets} distribution for a selection of $E_T \geq 150 \text{ GeV}$, $H_T \geq 400 \text{ GeV}$, $n_{\text{jets}} \geq 1$ and $n_{\text{btags}} \geq 1$. (d) n_{btags} distribution for a selection of $E_T \geq 150 \text{ GeV}$, $H_T \geq 400 \text{ GeV}$ and $n_{\text{jets}} \geq 4$.

4.1.4. Transverse Mass

In a two-body decay, the transverse mass is defined by the following equation [27]:

$$\begin{aligned} m_T^2 &= [E_{T,1} + E_{T,2}]^2 - [\vec{p}_{T,1} + \vec{p}_{T,2}]^2 \\ &= m_1^2 + p_{T,1}^2 + 2E_{T,1}E_{T,2} + m_2^2 + p_{T,2}^2 - p_{T,1}^2 - 2\vec{p}_{T,1} \cdot \vec{p}_{T,2} - p_{T,2}^2 \quad (4.3) \\ &= m_1^2 + m_2^2 + 2(E_{T,1}E_{T,2} - \vec{p}_{T,1} \cdot \vec{p}_{T,2}), \end{aligned}$$

where m_i , $E_{T,i}$ and $\vec{p}_{T,i}$ are the masses, the transverse energies and the transverse momenta of the daughter particles respectively. It can hence be measured without knowledge of momenta along the beam axis, i.e., in events with genuine \cancel{E}_T . The mass of the parent particle M is an upper bound to the transverse mass ($m_T \leq M$). Further discussion about the transverse mass variable is provided in Sec. 5.1 focussing on the transverse mass of the W boson.

4.2. Monte Carlo Simulation

Monte Carlo (MC) simulations serve different purposes. They are used to design the analysis strategy, produce a first estimate of the expected backgrounds and to verify background estimation techniques based on data. Furthermore, signal efficiencies and signal acceptance rates are calculated. Also, systematic errors are estimated with the help of simulated events.

Since a comprehensive simulation of all processes at the LHC in the CMS detector would not be feasible and many processes, which are not interesting for the analysis, are filtered by the trigger or the offline search selection, simulations are made for individual, selected processes of interest. The samples obtained from simulation are then combined with weights corresponding to the cross section of the appropriate background using

$$w = \frac{\sigma \mathcal{L}}{N}, \quad (4.4)$$

where σ is the cross section of the background process, \mathcal{L} the integrated luminosity of the data and N is the number of simulated events for each background sample. Another weight arises from the number of interactions in an event. In general, its distribution is different in simulation and real data. However, we require simulation to agree with data in this respect. Therefore, each event gets assigned a weight to correct for this distribution, which is then multiplied with the weight arising from the cross section of a sample.

The MC method is a discrete sampling of continuous distributions with different software packages. First, event generators, such as *Madgraph* and *Powheg* simulate the hard interaction. *Madgraph* is a next-to-leading order matrix element generator for high energy physics processes granting event generation [28]. *Powheg* is an event producer for hadronic processes with an approach based on perturbation theory truncated at next-to-leading order [29]. This step is followed by the fragmentation and showering of strongly interacting particles with *Pythia* [30]. The last steps include the decay of unstable hadrons into long-lived particles. *Tauola* handles the decay of tau leptons [31]. The resulting event is fed into the simulation of the detector using *Geant4*, which includes specific CMS characteristics such as geometry and materials [32]. After a simulated digitization step, the event reconstruction proceeds as if it were real data.

4.3. SM Backgrounds

Since SM processes are backgrounds in searches for new physics, it is essential to understand and to suppress them. In signal events, large missing transverse energy and high hadronic activity and a lepton is expected. This signature is found irreducibly in the following SM background processes:

- Top quark pair production as shown in Fig. 4.2 (a) ($t\bar{t}$),
- W boson production in association with jets (W+jets) and jets misidentified as b-jets,
- production of a single top quark decaying into a W boson and a b quark (single-top), and
- multijet production (QCD) with mismeasured jets providing \cancel{E}_T and a fake lepton.

4.3.1. The $t\bar{t}$ Background

The quantitatively largest background contribution arises from $t\bar{t}$ pair production followed by a semi-leptonic decay. The MC simulation samples used are:

- /TT_CT10_TuneZ2star_8TeV-powheg-tauola/Summer12_DR53X-PU_S10_START53_V7A-v1/AODSIM
- /TT_CT10_TuneZ2star_8TeV-powheg-tauola/Summer12_DR53X-PU_S10_START53_V7A-v2/AODSIM

In order to understand the classifications in the following sections, it is necessary to detail this process. In Fig. 4.2 (a) the Feynman diagram shows the production of a top

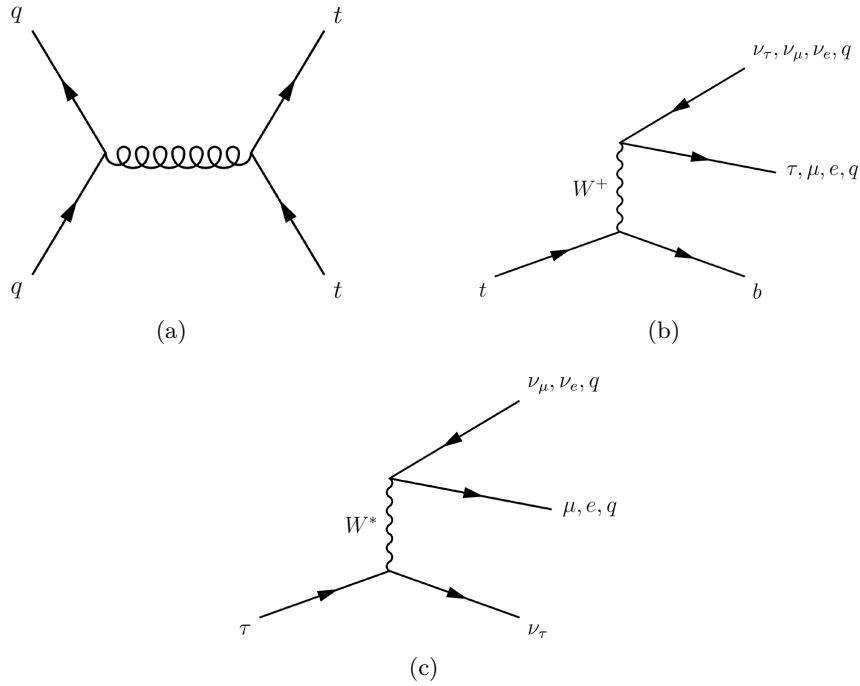


Figure 4.2.: Feynman diagrams of typical processes involved in $t\bar{t}$ pair production: (a) Quark-antiquark collision resulting in $t\bar{t}$ pair production. (b) Decay modes of the top quark. (c) Decay modes of the tau lepton.

quark and an antitop quark from the collision of two protons. The (anti) top quark decays into an (anti) b quark and a W^- (W^+) boson (Fig. 4.2 (b)). The W^+ (W^-) boson decays either hadronically into a quark-antiquark pair with a branching ratio of 67.6 %, or into a lepton-antilepton pair, which can be either an (anti) tau, (anti) muon or (anti) electron and the corresponding neutrino, respecting the conservation of the lepton number with a branching ratio of 10.8 % [27]. Tau leptons, in contrast to muons, decay immediately through a virtual off-shell W boson and a tau neutrino (Fig. 4.2 (c)). Again, the off-shell W boson yields either quarks, or a muon-antimuon neutrino pair, respectively an electron-antielectron neutrino pair. The two top branches and the W boson decays, as well as the decays of the tau leptons give many possible final states. They can be categorized into three main contributions:

- First, the all-hadronic contribution, where both top quark branches produce jets in their final states,
- the dileptonic contribution, where both top quark branches decay into leptonic states,

- the semi-leptonic (single leptonic) contribution, where one top quark branch always finalizes in a leptonic state, while the other always decays into quarks. This rate is calculated to $2 \cdot 0.108 \cdot (1 - 0.108) \approx 19.3\%$ using the above branching ratios.

These contributions will be treated individually in Sec. 5.2.

4.4. Event Selection

The analysis is performed with the CMS data set taken during proton-proton operations at $\sqrt{s} = 8$ TeV corresponding to an integrated luminosity of 20 fb^{-1} . In Tab. 4.1, the data samples used for this analysis are listed.

Table 4.1.: Data samples used for analysis

muons	\mathcal{L}
MuHad-Run2012A-13Jul2012	799 pb^{-1}
MuHad-Run2012B-13Jul2012	4.4 fb^{-1}
MuHad-Run2012C-Aug24ReReco	495 pb^{-1}
MuHad-Run2012C-PromptReco-v2	6.4 fb^{-1}
MuHad-Run2012D-PromptReco	7.3 fb^{-1}
electrons	\mathcal{L}
ElectronHad-Run2012A-13Jul2012	767 pb^{-1}
ElectronHad-Run2012B-13Jul2012	4.4 fb^{-1}
ElectronHad-Run2012C-Aug24ReReco	495 pb^{-1}
ElectronHad-Run2012C-PromptReco-v2	6.4 fb^{-1}
ElectronHad-Run2012D-PromptReco	7.3 fb^{-1}

In this single lepton analysis, muons and electrons, are required to fulfill specific selection criteria, in order to be identified as such, which are provided in the following subsections. The particle identification criteria necessitate the definition of certain variables. Leptons are required to be well isolated from other objects in order to reduce the misidentification rate. The accumulated transverse energies within the isolation cone divided by the transverse momentum of the lepton is henceforth called relative Isolation I_{rel} . The cone is of a size $\Delta R = \sqrt{(\Delta\eta)^2 + (\Delta\phi)^2} < 0.4$ for muons and $\Delta R < 0.3$ for electrons. The impact parameters, d_{xy} in the transversal plane, and d_z in beam direction, indicate the distance of an event's vertex from the primary vertex. They help to suppress undesired QCD events and events, in which the lepton does not originate from the primary collision vertex.

4.4.1. Muons

We distinguish between tracker muons, standalone muons and global muons. A tracker muon is a track with a hit in the inner tracking system, that has a match to the muon chambers. A standalone muon is a muon track fit accomplished in the muon chambers. A global muon is a standalone muon, that has an appropriate match in the inner tracking system.

A muon considered in the analysis has to be identified as global muon, in addition to being reconstructed as a muon by the particle flow algorithm [33]. The normalized χ^2 of the global-muon track fit is required to be ≤ 10 . At least one muon chamber hit included in the final track fit is necessary, that is matched to muon segments in at least two muon stations. Its corresponding tracker track must have more than five hits in the silicon tracker including at least one hit in the pixel detector. These criteria are listed in Tab. 4.2. Henceforth, a muon fulfilling these criteria is called a signal muon.

The requirements on “veto” muons are, by definition, lower. A veto muon must be reconstructed by the particle flow algorithm and must be identified either as a global muon or a tracker muon. Further requirements can be found in Tab. 4.2.

Table 4.2.: Additional requirements for well identified single lepton analysis muons and veto muons.

criterion	signal muon	veto muon
p_T	≥ 20 GeV	≥ 15 GeV
$ \eta $	≤ 2.4	≤ 2.5
I_{rel}	< 0.12	< 0.2
normalized χ^2	≤ 10	-
number of muon hits	> 0	-
number of matched stations	> 1	-
number of pixel hits	> 0	-
number of tracker layers with measurement	> 5	-
d_{xy}	< 0.02 cm	< 0.2 cm
d_z	< 0.5 cm	< 0.5 cm
$ p_T^{reco} - p_T^{pf} $	< 5 GeV	-

4.4.2. Electrons

Electron criteria are different for the barrel and endcaps regions of the detector. Accounting for the gap between the barrel and the endcaps, the region of $1.44 \leq |\eta| \leq 1.57$

is excluded from the electron identification. The quality requirements are separated in barrel requirements, in regions of $|\eta| < 1.44$, and endcap requirements $1.57 < |\eta| < 2.5$. The criteria are listed in Tab. 4.3. Such an electron will be called a signal electron. An electron fulfilling the requirements shown in the right-hand side columns in Tab. 4.3 is referred to as a veto electron.

Conversion rejection is a criterion to reject electrons, which arise from a photon decaying into an electron-positron pair. $\frac{H}{EM}$ is the ratio of the energy deposit in the hadronic calorimeter to the deposits in the electromagnetic calorimetric system. The $\sigma_{i\eta i\eta}$ variable characterizes the width of the supercluster. $\Delta\phi$ and $\Delta\eta$ are utilized for establishing the quality of the track-cluster matching process. They are sensitive to the quality of the spatial matching between the track and the supercluster. The transverse impact parameter, as well as the number of missing hits in the inner tracker layers are required to reject electrons arising from conversion [34].

Table 4.3.: Requirements for well identified single lepton analysis electrons and veto electrons.

criterion	signal electron		veto electron	
	barrel	endcaps	barrel	endcaps
p_T	≥ 20 GeV	≥ 20 GeV	≥ 15 GeV	≥ 15 GeV
$ \eta $	≤ 2.5	≤ 2.5	≤ 2.5	≤ 2.5
I_{rel}	< 0.15	< 0.15	< 0.15	< 0.15
$\frac{H}{EM}$	< 0.12	< 0.10	< 0.15	-
$ \Delta\phi $	< 0.06	< 0.03	< 0.8	< 0.7
$ \Delta\eta $	< 0.004	< 0.007	< 0.007	< 0.01
$\sigma_{i\eta i\eta}$	< 0.01	< 0.03	< 0.01	< 0.03
conversion rejection	yes	yes	-	-
number of missing hits	≤ 1	≤ 1	-	-
d_{xy}	< 0.02 cm	< 0.02 cm	< 0.04 cm	< 0.04 cm
d_z	< 0.1 cm	< 0.1 cm	< 0.2 cm	< 0.2 cm
$ p_T^{reco} - p_T^{pf} $	< 10 GeV	< 10 GeV	< 10 GeV	< 10 GeV

4.4.3. Single Lepton Channel

In the single lepton analysis, exactly one signal muon or electron is required, which will be referred to as the signal lepton. In order to prevent selecting dilepton events¹ from

¹Dilepton events are events of either two occurring muons, or two occurring electrons, or a muon and an electron.

$t\bar{t}$ production, no additional lepton in the veto selection is required.

The signal models considered in this search indicate the necessary kinematic selection: A tight lower bound on \cancel{E}_T for the single lepton channel of 150 GeV suppresses $t\bar{t}$ production with semi-leptonic decays, as well as QCD background events. The hadronic activity in signal events is high, which is the reason for requiring at least 400 GeV on H_T and at least 4 jets. Due to the decay of the top quark, also, a high b jet multiplicity is expected and we require at least one b-tagged jet.

4.5. QCD Background Yield Estimation

In this section, I perform a data-driven background estimation of the QCD multijet background. The simple procedure serves to illustrate the concepts used also in the later sections in a more complicated framework.

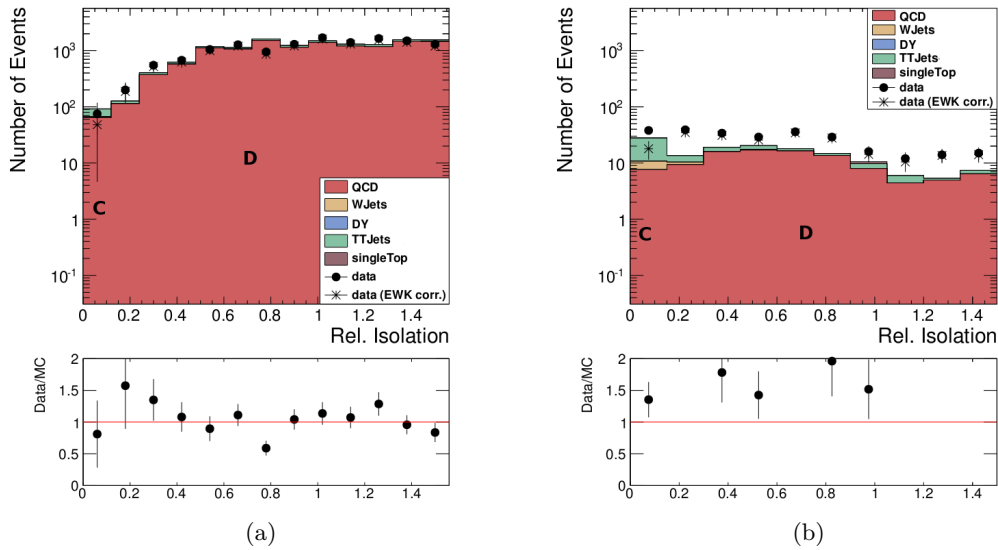


Figure 4.3.: Control regions (C and D) for: (a) muons (b) electrons

Since no prompt neutrinos are involved in QCD background events, the expected \cancel{E}_T is low, whereas H_T is expected to be high. The electron or muon is either provided from the decay of a bottom quark or from misidentification. By using a signal region selection of non zero missing energy, this background can be highly suppressed. Therefore, the requirement on the precision of the estimation is low. Upper limits for this process are calculated using the ABCD method. The ABCD method serves as an

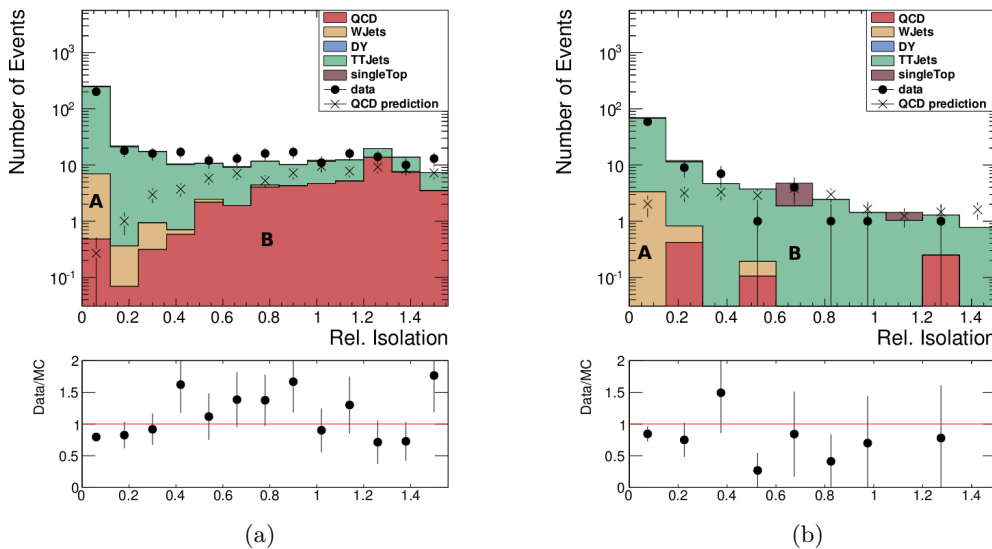


Figure 4.4.: QCD background estimation using the ABCD method. Signal regions (A) and I_{rel} sidebands (B) as well as the normalized control shapes are shown for: (a) muons with $150 \leq \cancel{E}_T < 250$ GeV and $1000 \leq H_T < 2500$ GeV. (b) electrons with $150 \leq \cancel{E}_T < 250$ GeV and $750 \leq H_T < 2500$ GeV.

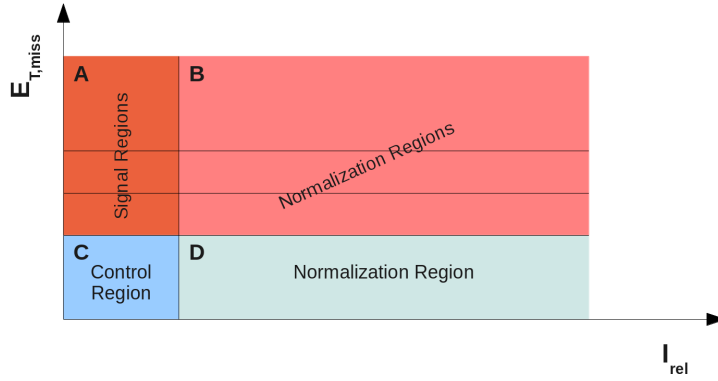
example of a data-driven background prediction.

The distribution of two uncorrelated variables is separated in four regions. Using the information from three regions, the background yield in the fourth region can be estimated by

$$\lambda_A = \frac{\lambda_C \lambda_B}{\lambda_D}, \quad (4.5)$$

where λ_i are the expectation values in the regions. In Fig. 4.5, a scheme of the regions used is depicted.

The estimation is based on loosening the requirement on the relative isolation I_{rel} in the selection of muons and electrons as well as an inversion of the impact parameter d_{xy} requirement. The region A, which is the to-be-estimated signal region, defined according to the ABCD method is given by the single lepton requirement $I_{rel} < 0.12$ and $I_{rel} < 0.15$ for muons and electrons, respectively, along with a high \cancel{E}_T requirement, depending on the signal region starting from $\cancel{E}_T \geq 150$ GeV. The I_{rel} shape is measured



(a)

Figure 4.5.: Scheme of the ABCD method and its regions.

in the QCD enriched control regions (C and D) in hadronically triggered data² and normalized in the sidebands of high relative isolation of the respective signal region (region B). The hadronically triggered data set is used in order to avoid a bias from the online isolation requirement for electrons and the prescales of low- H_T triggers are taken into account by weighting the measured events correspondingly. The enrichment of QCD in the control regions for muons is achieved by applying selections on the impact parameter and on \cancel{E}_T . An impact parameter of $0.01 < d_{xy} < 0.5$ cm and at least four jets with at least one of them being b-tagged are required. The missing transverse energy requirements are $\cancel{E}_T < 150$ for muons and $50 < \cancel{E}_T < 150$ GeV in the electron case. Two examples of I_{rel} control shapes are shown in Fig. 4.3.

The electron signal region for $400 < H_T < 750$ GeV and $250 < \cancel{E}_T < 2500$ GeV was estimated inclusively to avoid empty normalization regions. The number of estimated QCD events in the low \cancel{E}_T region ($150 < \cancel{E}_T < 250$ GeV) was scaled with the ratio between the electroweak background from simulation in the high \cancel{E}_T region and that in the low \cancel{E}_T region. Therefore, Tab. 4.4 shows only one value for this high \cancel{E}_T and low H_T region. Where applicable, the electroweak contribution as obtained from simulation (mostly W +jets and $t\bar{t}$ backgrounds), is subtracted. In summary, the contribution to the background from QCD multijet events is negligible for the considered signal regions [35].

²more details on the used data set can be found in Sec. A.1

Table 4.4.: Estimation on the QCD contribution in the ≥ 1 b-tag bin. The low H_T electron signal region (marked with *) corresponds to the inclusive bin $250 < \cancel{E}_T < 2500$ GeV. The regions of H_T in the first line are given in GeV.

muons	$400 \leq H_T < 750$	$750 \leq H_T < 2500$	$1000 \leq H_T < 2500$	
$150 \leq \cancel{E}_T < 250$ GeV	0.191 \pm 0.186	0.25 \pm 0.232	0.025 \pm 0.04	
$250 \leq \cancel{E}_T < 350$ GeV	0.004 \pm 0.019	0.012 \pm 0.024	0.007 \pm 0.012	
$350 \leq \cancel{E}_T < 450$ GeV	0.011 \pm 0.013	0.011 \pm 0.012	0.002 \pm 0.003	
$450 \leq \cancel{E}_T < 2500$ GeV	0.003 \pm 0.005	0.0 \pm 0.004	0.0 \pm 0.001	
electrons				
$150 \leq \cancel{E}_T < 250$ GeV	0.88 \pm 2.158	3.633 \pm 9.608	2.089 \pm 0.879	
$250 \leq \cancel{E}_T < 350$ GeV	0.099* \pm 0.242	0.0 \pm 0.217	0.087 \pm 0.093	
$350 \leq \cancel{E}_T < 450$ GeV	0.099* \pm 0.242	0.0 \pm 0.217	0.087 \pm 0.093	
$450 \leq \cancel{E}_T < 2500$ GeV	0.099* \pm 0.242	0.0 \pm 0.217	0.0 \pm 0.087	

5. Prediction of the Transverse Mass Distribution

This section discusses the background prediction of high transverse mass regions for a SUSY search in the single lepton channel with many jets, high transverse mass of the lepton- \cancel{E}_T system and a b-tag requirement. It introduces the transverse mass of the W boson, including the description of the various contributions of the $t\bar{t}$ background arising from the different decay channels of the top quarks. Two different approaches are pursued. The first uses simulated events to correct the distortion of the m_T shape based on two-dimensional templates. The second one performs an event-by-event correction carefully disentangling the different contributing subprocesses.

Since the relative normalizations and therefore the composition of backgrounds are obtained from simulations and subject to uncertainties, the predictions are restricted to the shapes of the individual distributions, while the normalization is free. The relative normalizations will be obtained from background dominated control regions by a Maximum Likelihood (MLL) fit procedure. For matters of quantification of the prediction, the predicted m_T shapes are normalized on the integrated yield of the simulated m_T distribution. The predictions are also done in simulation, which is also utilized to check and correct for residual biases.

5.1. The Transverse Mass of the W Boson

The dominant single leptonic backgrounds, which are described in Sec. 4.3 involve a W boson yielding the signal lepton (e or μ) and a neutrino. In particular, selecting high values of \cancel{E}_T and H_T suppresses other SM background models to a negligible level. In well reconstructed events, m_T has an endpoint at the W boson mass, at $m_W = 80.4$ GeV. Since the neutrino mass, the mass of the electron (511 keV/ c^2) and the mass of the muon (106 MeV/ c^2) are negligible compared to the energy scale of the event, we simplify Eq. (4.3) by $m_1 = m_2 = 0$. Applying this simplification leads to $E_{T,1} = p_{T,1} = \cancel{E}_T$ for the neutrinos and $E_{T,2} = p_{T,2}$ for the muon or electron. Equation (4.3) then reads

$$m_T^2 = 2 \cancel{E}_T p_{T,l} (1 - \cos(\Delta\phi)), \quad (5.1)$$

with the transverse momentum of the signal lepton $p_{T,l}$, the missing energy \cancel{E}_T of the event (dominated by the neutrino) and the azimuthal angle $\Delta\phi$ between them.

In SUSY decays, the correlation between \cancel{E}_T and the signal lepton is broken by the presence of the neutralinos. Since the direction of the two arising particles is independent of the lepton flight direction, the m_T distribution of SUSY signal events is different (Fig. 5.1). This is used to discriminate between the SM background and the SUSY signal.

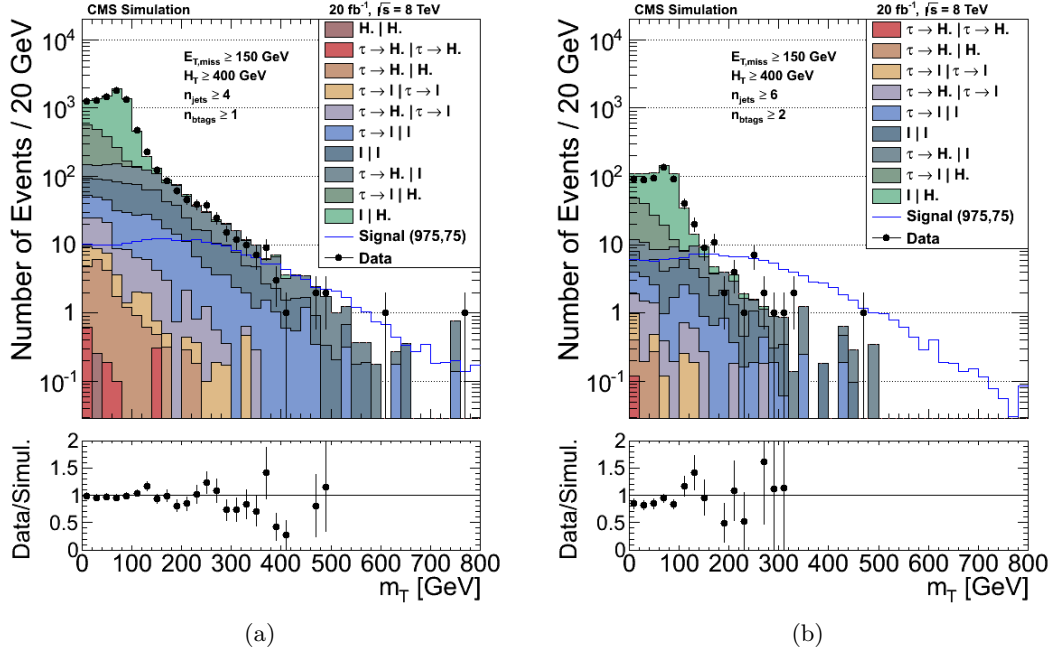


Figure 5.1.: The m_T distribution in the single lepton channel as obtained from simulation and compared to data. For comparison, a signal of $m_{\tilde{\chi}} = 975$ GeV and $m_{\tilde{\chi}} = 75$ GeV is overlaid. (a) shows the distribution for a selection of $\cancel{E}_T \geq 150$ GeV, $H_T \geq 400$ GeV, $n_{jets} \geq 4$ and $n_{btags} \geq 1$. (b) shows the distribution for a selection of $\cancel{E}_T \geq 150$ GeV, $H_T \geq 400$ GeV, $n_{jets} \geq 6$ and $n_{btags} \geq 2$. A comparison between figures (a) and (b) also reveals the increase of the signal to background ratio for a higher n_{jets} and n_{btags} requirement.

5.2. Contributions to the Transverse Mass Shape

Because of the various decay channels of $t\bar{t}$ and W +jets, \cancel{E}_T does not always only arise from the neutrino accompanying the signal lepton. In addition to a possible SUSY signal, \cancel{E}_T may arise from the following contributions to the single lepton channel:

- Tau leptons¹, yielding two tau neutrinos because of the conservation of the lepton number,
- a $t\bar{t}$ -jets dilepton event, where the second lepton, which arises in conjunction with its neutrino, fails the lepton veto requirement,
- a $t\bar{t}$ -jet dilepton event, where one or both of the leptons are tau leptons, yielding the corresponding number of tau neutrinos,
- errors in the p_T measurements in the detector, which are small compared to the other effects.

On the other hand misidentified leptons (jets reconstructed as leptons) do not arise with neutrinos. Therefore the expected \cancel{E}_T is higher than the measured one. These contributions to the missing energy cause a higher than nominal rate of events with $m_T > 80$ GeV.

According to the number and the flavor of neutrinos occurring in an event, a classification is done by using information from generator level, which, of course, is not available on real data. Starting from the case of a well reconstructed semi-leptonic $t\bar{t}$ event, the following list introduces the nomenclature of the contributions used in the figures within this thesis. The symbol “|” is used to separate the two top branches. On the two sides of the separator, the decay products of the respective W bosons are specified. Neutrinos are not specified in this nomenclature, since they are always created in conjunction with their non-neutrino leptonic partner, guaranteed by lepton number conservation. Henceforth, the regions of high values of m_T ($m_T \geq 120$) are called the m_T tail.

1. *Lepton|Hadrons (l|H.)*

With one muon or electron stemming from a W boson on one branch and a hadronic decay of the W boson on the other, this is the dominating background.

The m_T distribution has a sharp endpoint at m_W .

¹the mean lifetime of τ leptons is $\sim 3 \cdot 10^{-13}$ s

2. $\tau \rightarrow \text{Lepton}|\text{Hadrons}$ ($\tau \rightarrow l|H.$)

On one branch I find a τ lepton, that decays into an electron or muon via a virtual W boson. This yields two additional tau neutrinos contributing to \cancel{E}_T , but m_T is usually small (Fig. 5.1) and therefore the contribution to the tail is negligible.

3. $\tau \rightarrow \text{Hadrons}|\text{Lepton}$ ($\tau \rightarrow H.|l$)

These are dilepton events yielding the signal lepton on one branch and a tau lepton on the other. The tau lepton, though, decays hadronically contributing two tau neutrinos, which in turn contribute to the \cancel{E}_T . This channel is the largest contribution to the m_T tail.

4. $\text{Lepton}|\text{Lepton}$ ($l|l$)

Events of this category consist of two prompt leptons, one of which fails the veto selection requirements. Therefore, I call this lepton lost. There are different reasons, why leptons fail the veto selection requirements. The two most common reasons are either a shortfall of the p_T requirement, or a high value of the relative isolation. These two subcontributions reveal slightly different shapes in the prediction of the $\text{Lepton}|\text{Lepton}$ contribution.

5. $\tau \rightarrow \text{Lepton}|\text{Lepton}$ ($\tau \rightarrow l|l$)

These are dilepton events, where one lepton originates from a tau lepton. One of them is the signal lepton, the other one is lost. In these events, there are three additional neutrinos.

6. $\tau \rightarrow \text{Hadrons}|\tau \rightarrow \text{Lepton}$ ($\tau \rightarrow H.|\tau \rightarrow l$)

Two tau leptons are involved, one that decays into hadrons and one that decays into another lepton. In summary, this gives four extra neutrinos contributing to \cancel{E}_T .

7. $\tau \rightarrow \text{Hadrons}|\text{Hadrons}$ ($\tau \rightarrow H.|H.$)

Both W bosons decay into hadrons, one of which through the decay of a tau lepton. Thus, \cancel{E}_T solely arises from two tau neutrinos and jet mismeasurements.

8. $\tau \rightarrow \text{Lepton}|\tau \rightarrow \text{Lepton}$ ($\tau \rightarrow l|\tau \rightarrow l$)

Two leptons of this dileptonic event originate from tau leptons, which results in a total of 5 additional neutrinos and one lost lepton.

9. $\tau \rightarrow \text{Hadrons}|\tau \rightarrow \text{Hadrons}$ ($\tau \rightarrow H.|\tau \rightarrow H.$)

No prompt leptons are involved in the final states. Four neutrinos from two tau leptons result in \cancel{E}_T .

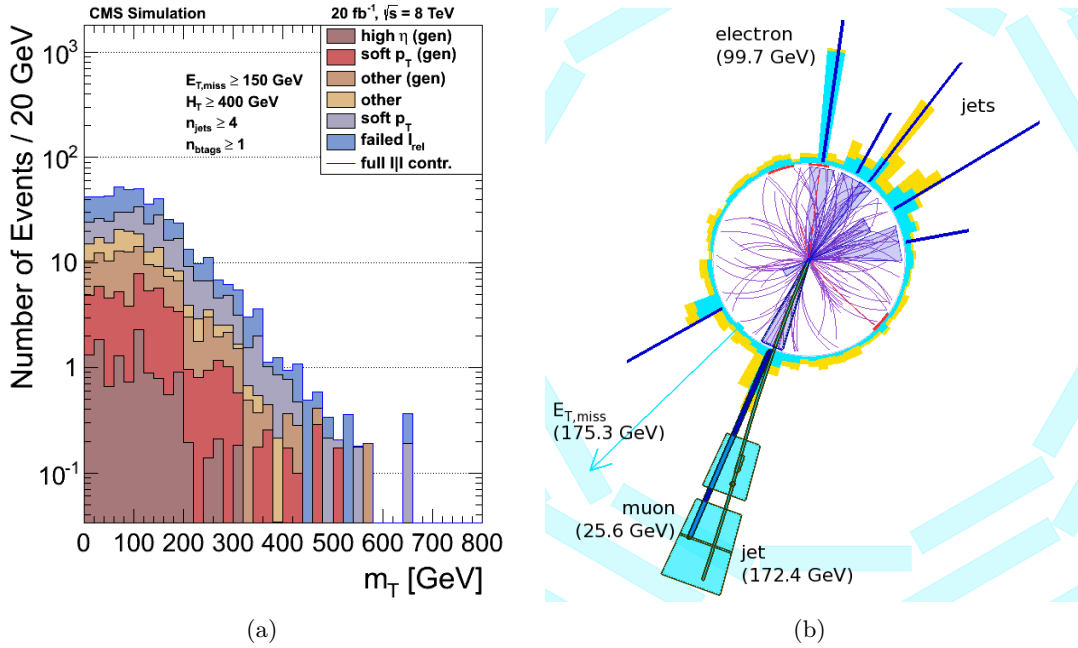


Figure 5.2.: The $Lepton|Lepton$ contribution: (a) shows subcontributions, due to high η , failed I_{rel} and soft p_T . The contributions marked with “gen” arise, when the according lepton was not reconstructed and instead generator information is used. “Other” contributions summarize contributions from leptons which fails the veto selection for other reasons than the given ones. (b) A $Lepton|Lepton$ event shown in the transverse plane of the CMS detector using the CMS Fireworks tool. The electron pointing upwards is the good signal lepton, whereas the muon pointing downwards was lost due to an overlap with a reconstructed jet.

10. $Hadrons|Hadrons$ ($H.|H.$)

Both W bosons decay into hadrons, with no genuine contribution to \cancel{E}_T . This is the reason for this contribution being the smallest after a preselection including an \cancel{E}_T requirement.

In Fig. 5.2 (a) all the subcontributions of $Lepton|Lepton$ events are shown. In Fig. 5.2 (b) a $Lepton|Lepton$ event is shown using the CMS Fireworks software [36]. The main contributions arise from the first four described processes. The two main contributions to the m_T tail, $\tau \rightarrow Hadrons|Lepton$ and $Lepton|Lepton$, make up at least 78% of the total background in the considered signal regions. We can design a data-driven background estimation for them and take the residual contributions from simulation.

5.3. Prediction of the Transverse Mass Distribution Using Correction Templates

This section discusses a simple estimation procedure based on two-dimensional templates. The previous section suggests, that events in the single lepton channel are likely to have high m_T if \cancel{E}_T receives contributions from additional neutrinos and lost leptons. The basic idea is to subtract the transverse momenta of these additional particles from the reconstructed \cancel{E}_T for each simulated event. The resulting \cancel{E}_T value describes the transverse momentum of the neutrino, that originates from the same W boson as the signal lepton, as well as detector mismeasurements. Recalculating m_T using this new value yields a distribution of m_T that resembles the *Lepton|Hadrons* contribution, i.e., the m_T distribution with no such effects present. We apply this procedure to the $\tau \rightarrow \text{Hadrons}|Lepton$ and the *Lepton|Lepton* contribution. Figure 5.3 shows the four major contributions before (a) and after (b) the correction.

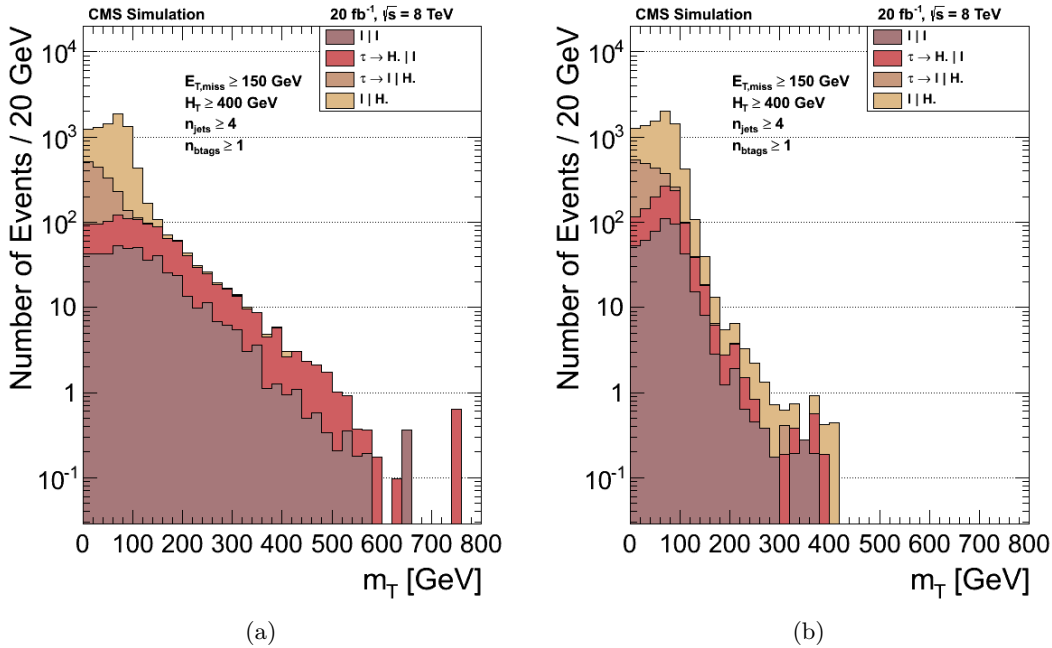


Figure 5.3.: The four major contributions to the m_T distribution: (a) shows m_T calculated with full reconstructed \cancel{E}_T . (b) shows m_T calculated after subtracting neutrinos from reconstructed \cancel{E}_T .

We now obtain a two dimensional distribution of m_T before and after the recalculation. Such histograms are shown in Fig. 5.4 for the two considered contributions.

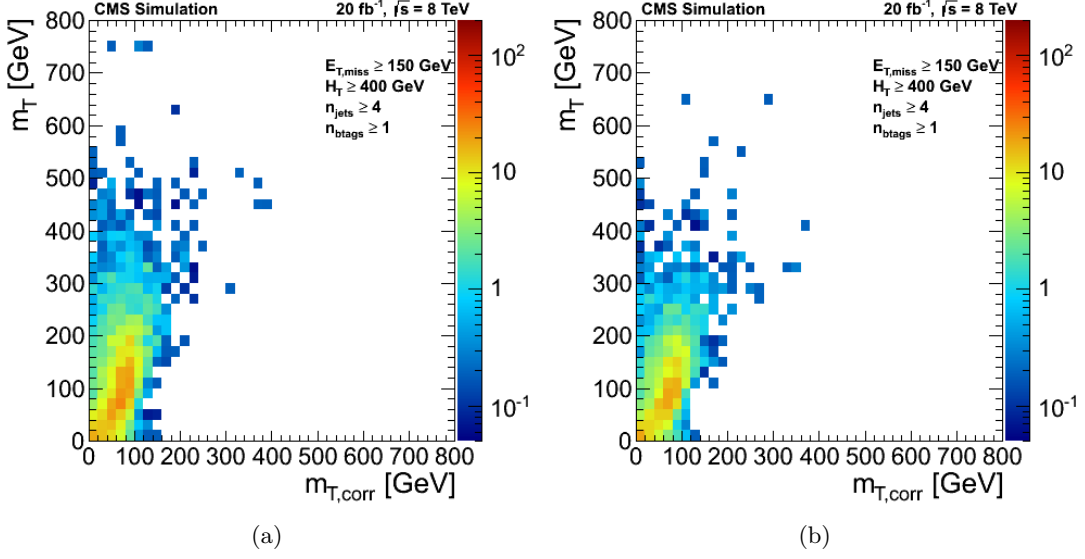


Figure 5.4.: Templates showing the correlation of m_T before (y -axis) and after (x -axis) the recalculation of \cancel{E}_T : (a) Template for the $\tau \rightarrow \text{Hadrons}|\text{Lepton}$ contribution. (b) Template for $\text{Lepton}|\text{Lepton}$ contribution.

The prediction is done as follows for the $\tau \rightarrow \text{Hadrons}|\text{Lepton}$ contribution. As a good approximation, the m_T shape in a low m_T region ($m_T \leq 100$ GeV) of the observed data is distributed as the $\text{Lepton}|\text{Hadron}$ contribution, since this is the dominating background in this region. Therefore, it is associated with the corrected m_T shape of the templates (x -axis). The $\tau \rightarrow \text{Hadrons}|\text{Lepton}$ contribution is associated with the y -axis of the $\tau \rightarrow \text{Hadrons}|\text{Lepton}$ templates. For each bin of the low m_T region of the x -axis of the templates, one can extract an m_T shape. Each of these shapes are weighted by the yield of observed data in the corresponding bin and then are summed up. The resulting distribution is the prediction for the $\tau \rightarrow \text{Hadrons}|\text{Lepton}$ contribution. This can be written as

$$P^i = \sum_{j=1}^m D^j \cdot W_T^{ij}, \quad (5.2)$$

where P^i is the prediction for each bin i , D^j is the data yield for each bin j and W_T^{ij} is the weight obtained from the applied template. The sum over all bins j ranges over the bins in the low m_T region, while i are the bins of the full m_T range. The prediction for the $\text{Lepton}|\text{Lepton}$ contribution is done analogously by using the $\text{Lepton}|\text{Lepton}$ template instead of the $\tau \rightarrow \text{Hadrons}|\text{Lepton}$ template.

The obtained shapes for both the $\tau \rightarrow \text{Hadrons}|\text{Lepton}$ and the $\text{Lepton}|\text{Lepton}$ con-

tribution, are area-normalized. In Tab. 5.1 and Tab. 5.2 the prediction yields for high regions of the m_T distribution are listed for several signal regions, while Fig. 5.5 shows a comparison between prediction and simulation for the regions with the requirements $\cancel{E}_T \geq 150$ GeV, $H_T \geq 400$ GeV, $n_{jets} \geq 4$ and $n_{btags} \geq 1$.

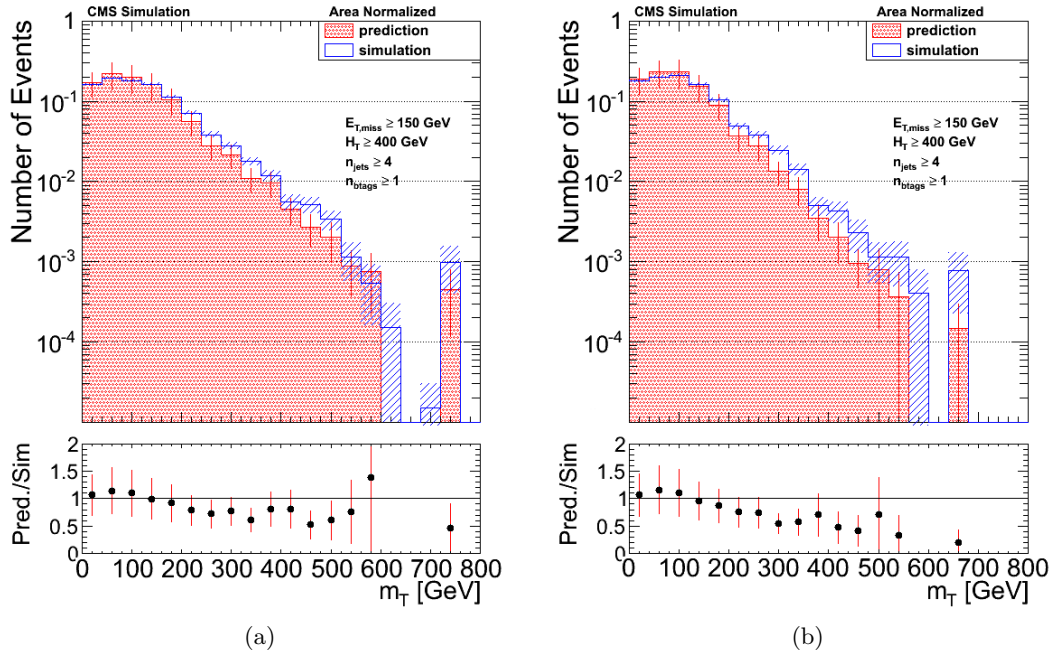


Figure 5.5.: Prediction using correction templates for the (a) $\tau \rightarrow \text{Hadrons}|\text{Lepton}$ contribution and the (b) $\text{Lepton}|\text{Lepton}$ contribution for a selection $\cancel{E}_T \geq 150$ GeV, $H_T \geq 400$ GeV, $n_{jets} \geq 4$ and $n_{btags} \geq 1$.

This kind of prediction is strongly dependent on the first bins of the m_T distribution. In this region, there are only small differences between the MC simulation and the observed data. Thus, the predicted yields in both cases are fairly similar. Furthermore, the templates have great uncertainties, as well as they are quite inflexible. However, their application is fast and in this regard they are sufficient to motivate further attempts with more flexible methods and smaller uncertainties.

5.4. Single Lepton Prediction of the Transverse Mass Distribution from Dilepton Events

Since both of the largest contributions to m_T ($\tau \rightarrow \text{Hadrons}|\text{Lepton}$, $\text{Lepton}|\text{Lepton}$) involve two leptons (one for each decaying W boson), it is possible to use dilepton

Table 5.1.: Prediction for m_T tail of the hadronic tau contribution using correction templates for different signal regions. The table does not show the statistical uncertainties from MC.

\cancel{E}_T [GeV]	H_T [GeV]	n_{jets}	n_{btags}	MC	pred. from MC		pred. from data	
150	400	4	1	302.2	263.9	\pm 49.3	264.8	\pm 49.3
150	400	6	1	38.5	34.4	\pm 7.0	34.5	\pm 7.0
150	400	6	2	19.1	17.3	\pm 4.4	17.6	\pm 4.5
150	750	4	1	64.6	55.5	\pm 10.6	56.0	\pm 10.8
150	750	6	2	8.0	7.2	\pm 2.1	7.4	\pm 2.2
250	400	4	1	66.3	56.7	\pm 9.4	56.2	\pm 9.3
250	400	6	2	4.2	3.5	\pm 1.5	3.4	\pm 1.4
250	750	4	1	24.3	20.7	\pm 3.8	20.1	\pm 3.7
250	750	6	1	5.7	5.1	\pm 1.3	5.0	\pm 1.2
250	750	6	2	2.7	2.3	\pm 0.9	2.3	\pm 1.0

events to predict the shapes of these contributions. The dilepton data sets used for the prediction can be found in the appendix. The expected \cancel{E}_T of dilepton events and the $Lepton|Lepton$ contribution agrees well, since $Lepton|Lepton$ events, in fact are dilepton events. The expected \cancel{E}_T of dilepton events and the $\tau \rightarrow Hadrons|Lepton$ contribution differs only by one additional tau neutrino from the decay of the tau lepton. The basic idea for a single lepton channel prediction for these contributions is to measure \cancel{E}_T from dilepton events and calculate m_T from it. In the $\tau \rightarrow Hadrons|Lepton$ case, a correction on the dilepton \cancel{E}_T is made accounting for the two additional neutrinos. The $Lepton|Lepton$ contribution is split into its two largest subcontributions, whose \cancel{E}_T are predicted using appropriate selections on the dilepton sample.

5.4.1. The $\tau \rightarrow Hadrons|Lepton$ contribution

Considering the $\tau \rightarrow Hadrons|Lepton$ contribution, \cancel{E}_T in dilepton events lacks the contribution of the tau neutrino, that comes from the hadronic decay of the tau lepton. Since the tau lepton decays into hadrons, there is one lepton in the final states in this contribution, whereas dilepton events have two leptons in their final states involved. On the other hand, n_{jets} is usually higher than in dilepton events.

In order to account for this additional \cancel{E}_T contribution, templates of the transverse momentum of the tau neutrino are created in bins of the tau lepton's momentum and pseudo rapidity (p_T^τ, η^τ). The information about the direction of the tau neutrino in the transverse plane (ϕ^τ) is encoded in the transverse momentum of the tau neutrino in the coordinate system of the tau lepton flight direction. In principle, the templates

CHAPTER 5. PREDICTION OF THE TRANSVERSE MASS DISTRIBUTION

Table 5.2.: Prediction for m_T tail of the lost lepton contribution using correction templates for different signal regions. The table does not show the statistical uncertainties from MC.

\cancel{E}_T [GeV]	H_T [GeV]	n_{jets}	n_{btags}	MC	pred. from MC		pred. from data		
150	400	4	1	192.5	159.9	\pm 31.4	160.6	\pm 31.4	
150	400	6	1	19.6	16.2	\pm 4.3	16.3	\pm 4.3	
150	400	6	2	10.8	8.6	\pm 2.3	8.7	\pm 2.3	
150	750	4	1	39.4	31.2	\pm 6.4	31.6	\pm 6.5	
150	750	6	2	4.8	4.1	\pm 1.3	4.2	\pm 1.3	
250	400	4	1	40.2	30.2	\pm 5.2	29.8	\pm 5.2	
250	400	6	2	2.3	1.7	\pm 0.6	1.7	\pm 0.6	
250	750	4	1	15.9	11.1	\pm 2.3	10.7	\pm 2.2	
250	750	6	1	3.8	3.1	\pm 1.0	2.9	\pm 0.9	
250	750	6	2	2.2	1.6	\pm 0.6	1.7	\pm 0.7	

are two dimensional. One component indicates the transverse momentum of the tau neutrino in the projection parallel to the tau lepton flight direction ($\cancel{E}_{T\parallel}^\tau$), and one in the orthogonal projection ($\cancel{E}_{T\perp}^\tau$). The momentum of the tau neutrino in the orthogonal projection is constrained by $\pm m_\tau/2 = \pm 0.9/2$ GeV. Since this value is small compared to the p_T scale in this selection, we simplify the calculation by omitting this orthogonal component. In Fig. 5.6, representative tau templates are shown, Fig. 5.6 (b) shows a two dimensional template to disclose the relation between the orthogonal component and the tau lepton mass.

The dilepton events used for the prediction are selected as follows: A signal lepton is required, along with one reconstructed muon or electron satisfying a looser selection defined by a reduced p_T threshold of 10 GeV. This loosening serves to reduce a kinematical bias of the ensuing prediction. The prediction is then done by assuming, that the looser lepton is a tau lepton. If both of the dileptons in an event satisfy $p_T \geq 20$ GeV, the event is used twice, once for each lepton.

Then, the prediction is performed. The correct template (T_τ) is chosen, according to p_T^τ and η^τ . For each bin i of $\cancel{E}_{T\parallel i}^\tau$ of the template, the corrected \cancel{E}_T ($\cancel{E}_{T,i}^{corr}$) is calculated using the genuine \cancel{E}_T of the dilepton event (\cancel{E}_T^{DL}) as

$$\cancel{E}_{T,i}^{corr} = \sqrt{\left[\cancel{E}_{T,x}^{DL} + \cancel{E}_{T\parallel i}^\tau \cos(\phi^\tau)\right]^2 + \left[\cancel{E}_{T,y}^{DL} + \cancel{E}_{T\parallel i}^\tau \sin(\phi^\tau)\right]^2}, \quad (5.3)$$

and weighted with

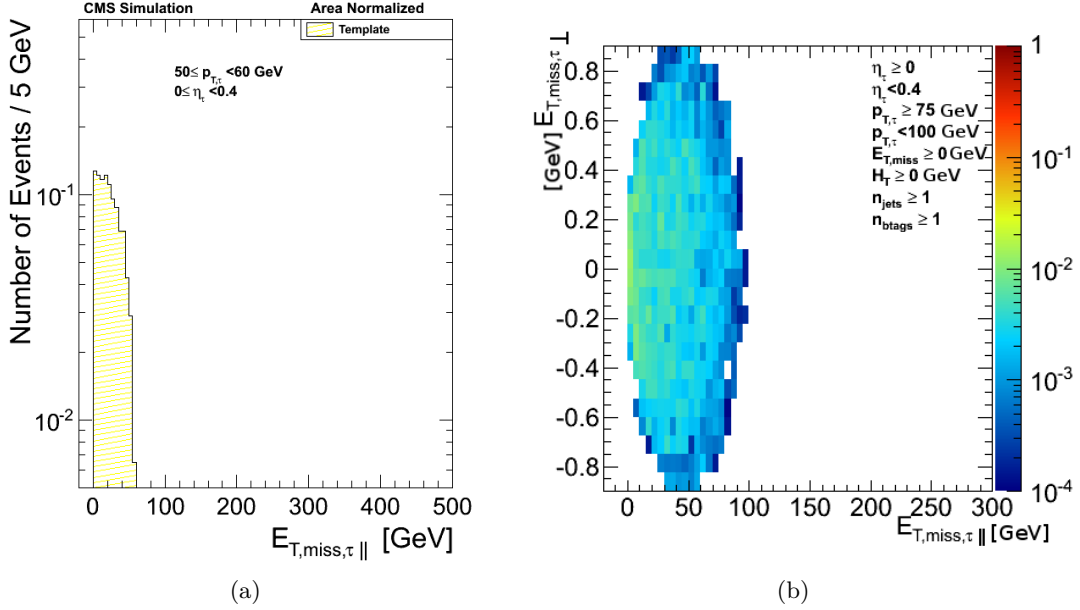


Figure 5.6.: Tau templates: (a) Tau template for a lepton with $50 \leq p_T^\tau < 60$ GeV, $0 \leq \eta_\tau < 0.4$ as it is used in the $\tau \rightarrow \text{Hadrons}|\text{Lepton}$ prediction. (b) Two dimensional template showing the momentum of the tau neutrino in direction of the tau lepton on the x axis and the momentum of the tau neutrino in direction orthogonal to the tau lepton on the y axis. The limiting factor of the y component is the tau lepton mass ($\pm \frac{m_\tau}{2} = \pm \frac{0.9}{2}$). This template is shown for a lepton with $75 \leq p_T^\tau < 100$ GeV, $0 \leq \eta_\tau < 0.4$.

$$W_i = \frac{T_i}{\sum_j T_j}, \quad (5.4)$$

where T_i are the yields of each bin of the utilized template. The predicted m_T shape is obtained from calculating m_T using $\cancel{E}_{T,i}^{corr}$, which is depicted in Fig. 5.7 (a). It shows that the simulated $\tau \rightarrow \text{Hadrons}|\text{Lepton}$ contribution agrees well with the one predicted from dilepton events.

Several observables of the predicted sample are corrected in order to allow unbiased requirements. There is usually an additional reconstructed jet in tau events if it decays hadronically. The jet multiplicity in the event is increased by one, if $|\vec{p}_T^\tau - \vec{p}_T^{\nu_\tau}| \geq 40$ GeV, by which the H_T is increased in this case. This defines n_{jets}^{Corr} and H_T^{Corr} which are used for making selections on the prediction. The influence of this correction is compared in Fig. 5.7 (b). Despite the fact that the distribution of m_T is not strongly affected by the corrections to H_T and n_{jets} , it is important to perform these corrections

for a realistic modelling of the kinematical properties. This can be seen in the n_{jets} distribution in Fig. 5.8 (a). In Fig. 5.8 (b) and (c) the distributions of, H_T and \cancel{E}_T are shown comparing the prediction to simulation.

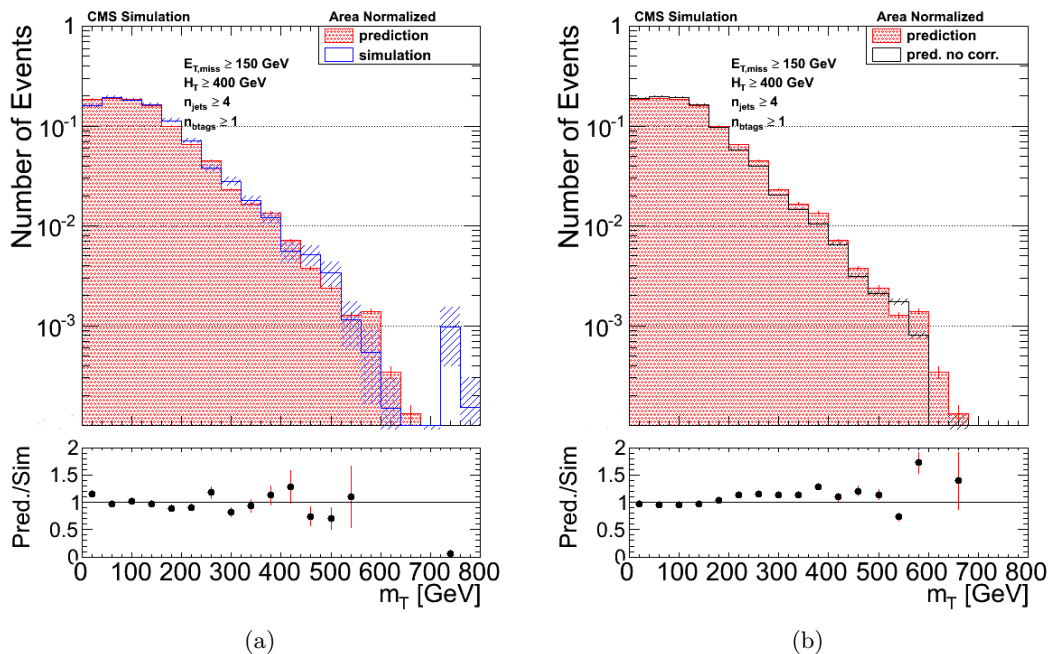


Figure 5.7.: Prediction of the $\tau \rightarrow Hadrons|Lepton$ distribution from dilepton events for a signal region $\cancel{E}_T \geq 150$ GeV, $H_T \geq 400$ GeV, $n_{jets} \geq 4$ and $n_{btags} \geq 1$: (a) Distribution of the predicted m_T compared to the simulated m_T . (b) Distribution of the predicted m_T compared to the shape of the prediction without H_T and n_{jets} correction binned in m_T .

In order to quantify the predictions before the fit is done, the predicted m_T distribution was normalized to the integrated yield of the simulated m_T distribution. The proper relative normalizations are obtained from the fit on data later as described in Sec. 6.1. Table 5.3 lists the yields of predictions of high values of the transverse mass ($m_T \geq 120$ GeV).

5.4.2. The $Lepton|Lepton$ Contribution

As described in Sec. 5.2, the $Lepton|Lepton$ background consists of several contributions, which in general have different shapes. On the one hand, the $Lepton|Lepton$ contribution arises from dilepton events and requirements on one of the leptons leads to a suitable prediction in each case. On the other hand, the requirement on precision is not high, as the regarding contributions are subleading. Therefore, it is sufficient

Table 5.3.: Prediction for the m_T tail of the hadronic tau contribution using dilepton events and different signal regions. The table does not show the statistical uncertainties from MC.

\cancel{E}_T [GeV]	H_T [GeV]	n_{jets}	n_{btags}	MC	pred. from MC	pred. from data
150	400	4	1	302.2	284.8 ± 0.6	287.3 ± 1.5
150	400	6	1	38.5	34.6 ± 0.2	35.7 ± 0.5
150	400	6	2	19.1	16.6 ± 0.1	15.0 ± 0.3
150	750	4	1	64.6	56.9 ± 0.3	56.0 ± 0.7
150	750	6	2	8.0	7.5 ± 0.1	6.5 ± 0.2
250	400	4	1	66.3	62.6 ± 0.3	60.5 ± 0.6
250	400	6	2	4.2	3.3 ± 0.1	3.3 ± 0.1
250	750	4	1	24.3	22.7 ± 0.2	18.8 ± 0.3
250	750	6	1	5.7	5.0 ± 0.1	7.3 ± 0.2

to estimate only the two major subcontributions, which are, as stated in Sec. 5.2, the high- I_{rel} contribution $C_{I_{rel}}$ and the low- p_T contribution C_{p_T} . The full $Lepton|Lepton$ contribution C_{ll} is then composed of these two predictions in addition to a small residual contribution, which contains the remaining processes and which is fully taken from simulations. The sum can be written as

$$C_{ll} = N_{I_{rel}}^{MC} S_{I_{rel}}^{pred}(m_T) + N_{p_T}^{MC} S_{p_T}^{pred}(m_T) + N_{other}^{MC} S_{other}^{MC}(m_T) = N_{ll} S_{ll}(m_T), \quad (5.5)$$

where N denotes the normalizations and $S(m_T)$ the shapes. In order to quantify the prediction before the fit is done, the normalizations correspond to the integrated yield of the simulated m_T distribution. In Sec. 6.1, the relative normalizations are obtained from a fit on data.

The strategy of prediction for the high- I_{rel} fraction is to select dilepton events with one signal lepton and another electron or muon passing looser signal lepton criteria defined by requiring a transverse momentum of only $p_T \geq 15$ GeV.

For the low- p_T prediction, one good signal lepton and another electron or muon passing the looser signal lepton criteria with $p_T \geq 10$ GeV. In order to gain more events for the prediction, but not to overlap with the high- I_{rel} contribution, events in which the loose lepton fulfills $p_T \geq 15$ GeV are used in the following way. The lepton transverse momentum is added to the \cancel{E}_T vectorially, which simulates a soft lepton and a neutrino carrying away the p_T . The shapes of both predicted subcontributions compared to simulation, as well as the total $Lepton|Lepton$ contribution according to

Eq. (5.5) are depicted in Fig.5.9. Table 5.4 shows the yields of C_U for the m_T tail considering different signal regions.

Table 5.4.: Prediction for the m_T tail of the lost lepton contribution from dilepton events for different signal regions. The table does not show the statistical uncertainties from MC.

\cancel{E}_T [GeV]	H_T [GeV]	n_{jets}	n_{btags}	MC	pred. from MC		pred. from data	
150	400	4	1	192.5	182.9	± 7.7	177.8	± 6.0
150	400	6	1	19.6	21.1	± 2.7	22.4	± 2.4
150	400	6	2	10.8	10.4	± 1.8	8.2	± 1.5
150	750	4	1	39.4	33.2	± 2.8	33.8	± 2.7
150	750	6	2	4.8	5.6	± 1.4	4.5	± 1.1
250	400	4	1	40.2	35.9	± 3.7	31.6	± 2.5
250	400	6	2	2.3	1.4	± 0.4	0.2	± 0.1
250	750	4	1	15.9	11.9	± 1.6	7.4	± 1.4
250	750	6	1	3.8	3.4	± 1.3	4.3	± 2.9

5.5. Systematic Uncertainties on the Predictions

The systematic uncertainty on the $\tau \rightarrow Hadrons|Lepton$ prediction is an uncertainty on the predicted m_T shape and is obtained in the following way: The relative uncertainty is obtained by normalizing the predicted shape on the first bin equalling 1. After the uncertainty on the first bin is quadratically added to the remaining bins, these uncertainties are the relative systematic errors for each bin of the prediction and are later transferred to the MLL fit. This kind of uncertainties is henceforth referred to as “shape uncertainty”.

The systematic uncertainties on the $Lepton|Lepton$ contribution originate from two sources: One stems from the statistical uncertainties of the prediction and is calculated analogously to the shape uncertainty of the $\tau \rightarrow Hadrons|Lepton$ contribution. The other results from the relative fractions of the $Lepton|Lepton$ subcontributions, rather their not well known relative normalization. Therefore, I perform a random sampling of the simulated fractions using large uncertainties on the relative fractions. This procedure is feasible, since the contributing shapes are sufficiently similar. Sticking to the notation from Eq. (5.5), each of the N_i are multiplied by random values following a log-normal distribution of mean 1 and variance 0.5. The obtained C_U is normalized on the first bin to yield 1. This is repeated sufficiently often (1000 times), which results in different contributions per m_T bin, of which the standard deviation and mean

is calculated for each bin. The relative uncertainty per bin results in the henceforth called “composition uncertainty”. The shape uncertainties and the composition uncertainties of the $Lepton|Lepton$ contribution are added up quadratically, since they are not correlated.

5.6. MC Simulation Prediction Correction Factors

The predicted shapes from simulations and the simulation itself ought to agree. However, their distributions slightly differ, because of the simplifying assumptions they were obtained under. This gives rise to a correction. We introduce a shape correction factor K_i for each bin i , defined by

$$K_i = \frac{Y_i^{MC}}{Y_i^{[pred,MC]}} \quad (5.6)$$

for the yield Y in bin i , where $[pred, MC]$ denotes the prediction obtained from simulation.

K_i is applied to correct the predictions from data as follows:

$$Y_i^{pred,K} = Y_i^{pred} K_i \quad (5.7)$$

The values of the K-factors for the $\tau \rightarrow Hadrons|Lepton$ contribution, as well as the $Lepton|Lepton$ contribution for a signal region $\cancel{E}_T \geq 150$ GeV, $H_T \geq 400$ GeV, $n_{jets} \geq 4$ and $n_{btags} \geq 1$ are shown in Fig. 5.10. Their uncertainties correspond to the shape uncertainties described in Sec. 5.5.

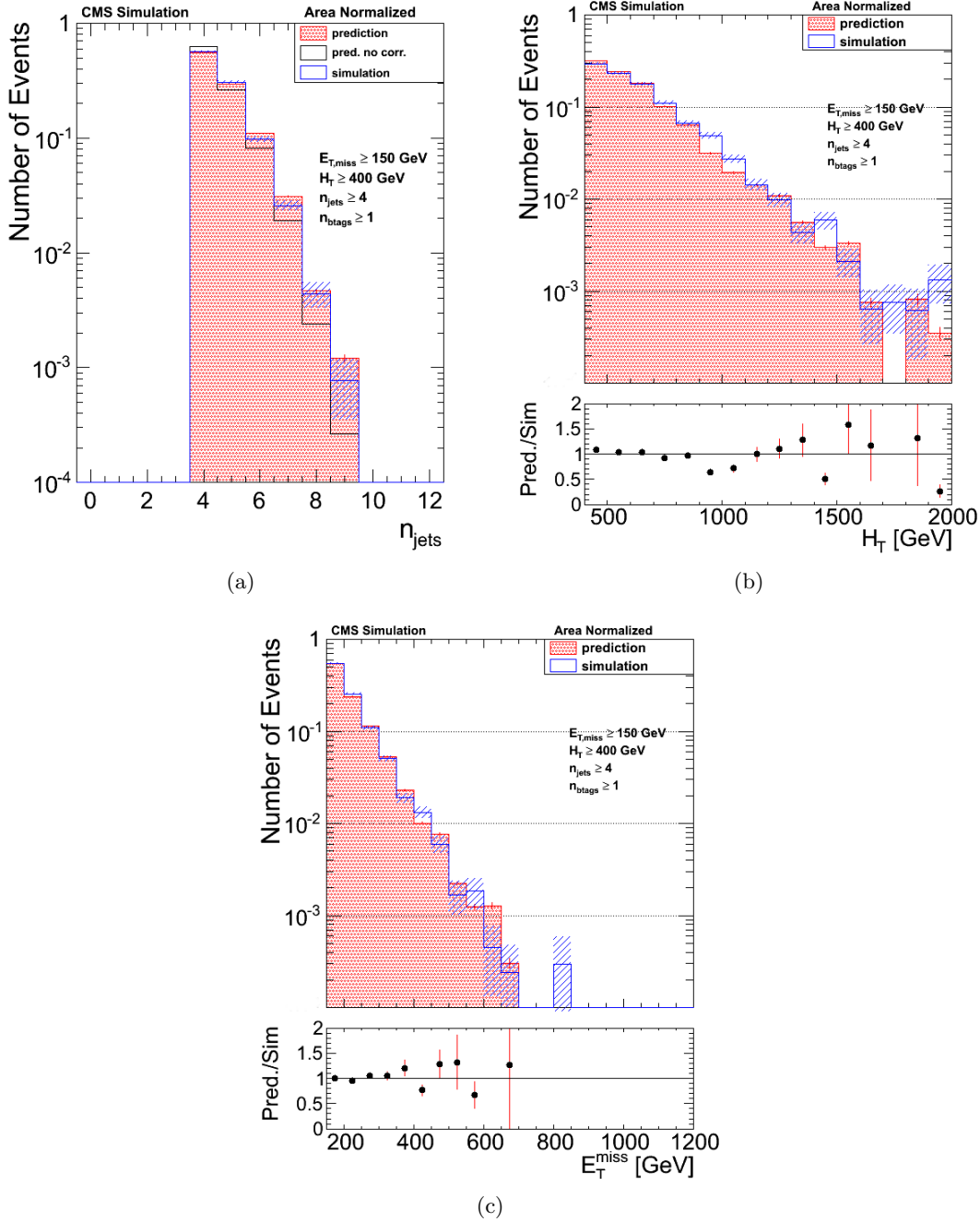


Figure 5.8.: Prediction of the $\tau \rightarrow Hadrons|Lepton$ shape from dilepton events for a signal region $E_{T,miss} \geq 150$ GeV, $H_T \geq 400$ GeV, $n_{jets} \geq 4$ and $n_{btags} \geq 1$: (a) Distribution of n_{jets} of the prediction compared to simulation and the prediction without the corrections in n_{jets} and H_T . It can be seen that the distributions of the jet multiplicity are well agreeing after a simple correction in n_{jets} and H_T . (b) Distributions of H_T of the prediction compared to simulation. (c) Distributions of $E_{T,miss}$ of the prediction compared to simulation binned.

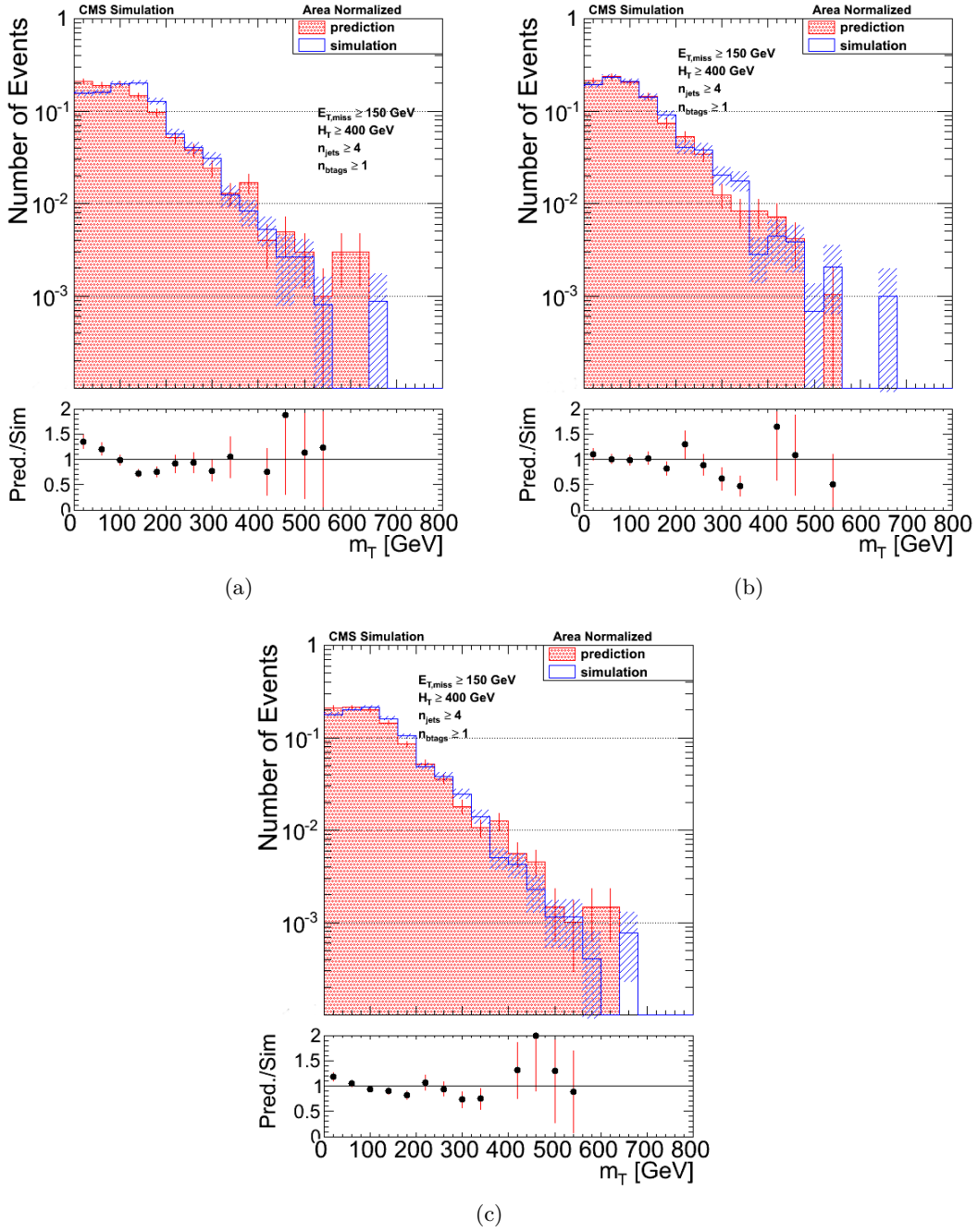


Figure 5.9.: Prediction of the $Lepton|Lepton$ distribution from dilepton events for a signal region $E_T \geq 150$ GeV, $H_T \geq 400$ GeV, $n_{jets} \geq 4$ and $n_{btags} \geq 1$: (a) Shape of the prediction of the high- I_{rel} subcontribution compared to the shape of its simulation. (b) Shape of the prediction of the low- p_T subcontribution compared to the shape of its simulation. (c) Shape of the summed up predictions as described by Eq. (5.5) compared to the $Lepton|Lepton$ shape obtained from simulation.

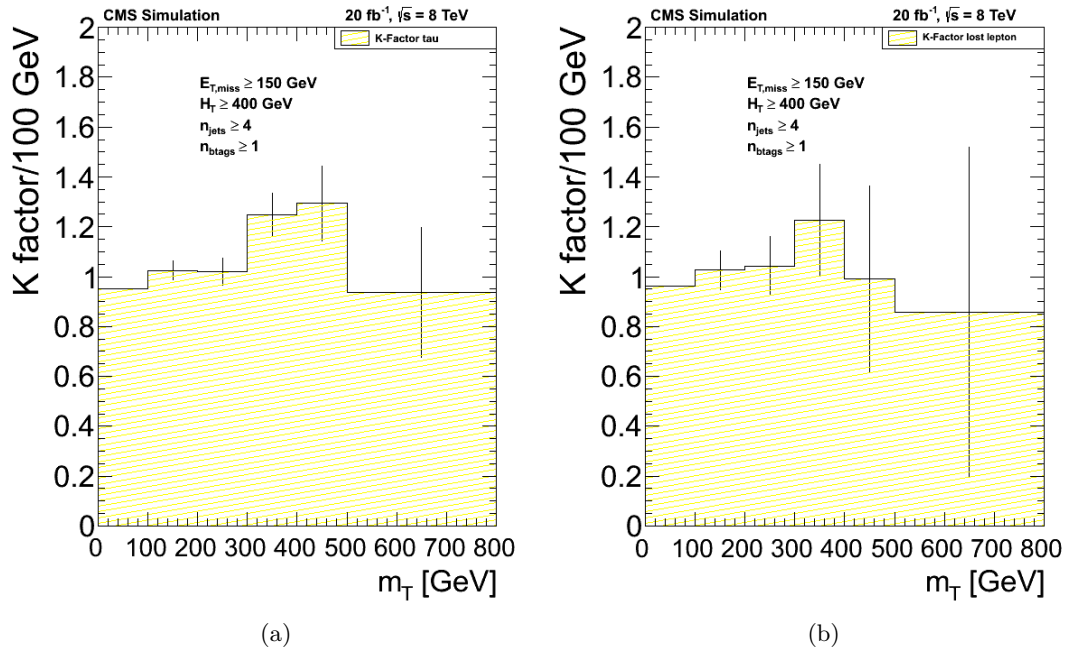


Figure 5.10.: K-factors for the region $\cancel{E}_T \geq 150 \text{ GeV}$, $H_T \geq 400 \text{ GeV}$, $n_{\text{jets}} \geq 4$ and $n_{\text{btags}} \geq 1$. The binning in 100 GeV steps is chosen, as it will be used for the fit and limit calculation procedure. (a) $\tau \rightarrow \text{Hadrons}|\text{Lepton}$ contribution. (b) $\text{Lepton}|\text{Lepton}$ contribution.

6. Results

This section provides the final results of this thesis. The final result of a search for new physics is either the discovery or the exclusion of the model parameters, that parametrize a model of new physics. No discovery was achieved so far and exclusion limits are calculated using the so-called CL_s method. A MLL fit of the predictions on data is done using a specific model, which serves to describe the background in bins of m_T . At the end of this section the exclusion limits are presented and interpreted within the introduced simplified models spectrum.

6.1. Maximum Likelihood Fit

A fit of our predictions on data is necessary for two reasons. First, background dominated channels allow the fit to determine the normalizations of the floating background components. Secondly, the quality of the fit validates, how well the data is described by the background model and therefore is an important factor in the decision, whether the model is applicable. A minimum of the following properties of the applied model needs to be specified:

- The observation for each bin of the m_T variable.
- The yields of the prediction from data corrected by the K -factors for each bin of the m_T variable. This includes the background dominated low- m_T regions serving as control regions, in order to constrain the normalizations.
- The signal hypothesis for each bin of the m_T variable: Considering the simplified models, the model parameters are the mass of the gluino $m_{\tilde{g}}$, the mass of the stop quark $m_{\tilde{t}}$ and the mass of the lightest supersymmetrical particle LSP, the neutralino $m_{\tilde{\chi}}$. Thus, for each of the three applied simplified models and for each possible combination of respectively two of these particle masses, a different cross section and therefore a different signal is expected.
- The prediction's systematic uncertainties obtained as described in Sec. 5.5, serving as the boundaries of the nuisance parameters in the MLL fit.

- The full correlation pattern among all contributions and across all bins.

6.1.1. Signal Binning

This necessitates the introduction of a signal binning as follows. The fit is performed in the regions of $\cancel{E}_T \geq 150$ GeV, $H_T \geq 400$ GeV and $n_{btags} \geq 1$, once for $n_{jets} \geq 4$ and once for $n_{jets} \geq 6$. In the $n_{jets} \geq 4$ case, m_T is binned in a 100 GeV interval on a scale from 0 to 500 GeV. The sixth, last bin contains all events of $m_T \geq 500$ GeV. In the $n_{jets} \geq 6$ case, m_T is binned in a 100 GeV interval up to 400 GeV, while the fifth bin contains all events of $m_T \geq 400$ GeV. In both cases the first bin corresponds to the background dominated control region.

6.1.2. The Fit Model

The fit model consists of three fractions:

1. The predicted $\tau \rightarrow Hadrons|Lepton$ shape $S_\tau^{pred}(m_T)$ normalized to the value obtained from simulation N_τ^{MC} : $C_\tau = S_\tau^{pred}(m_T)N_\tau^{MC}$,
2. the predicted $Lepton|Lepton$ shape $S_{ll}^{pred}(m_T)$ normalized to the value obtained from simulation N_{ll}^{MC} : $C_{ll} = S_{ll}^{pred}(m_T)N_{ll}^{MC}$,
3. all the remaining contributions, which are the two largest contributions, as well as the minor tail contributions fully taken from simulation $C_m = S_m^{MC}(m_T)N_m^{MC}$.

The full model for the predicted background yield in bin is

$$BG^i = R_{bg} \left[C_m^i + R_{\tau,ll} \left(C_\tau^i R_\tau^i + C_{ll}^i R_{ll}^i \right) \right] \quad (6.1)$$

The multipliers \mathbf{R} are the nuisance parameters and can be understood as the background normalization factors, which are injected as 1 with a large uncertainty, which leaves them effectively floating. These uncertainties correspond to the systematic uncertainties originating from the prediction, as well as to the unknown normalization of the predicted shapes. They define the lower and upper limits the nuisance parameters can achieve in the fit process.

R_{bg} represents the normalization of the full background model, which affects all three fractions. We allow R_{bg} to float freely between 0.5 and 2, by assigning the nuisance parameter an uncertainty of 100%, that is log-uniform distributed. $R_{\tau,ll}$ affects only the two tail contributions. Again, a 100% log-uniform distributed uncertainty on this parameter allows free floating in a range of 0.5 and 2. We assign these large

uncertainties to R_{bg} and $R_{\tau,ll}$ in order to constrain the normalization relying on the correlation between the channels. R_{τ}^i and R_{ll}^i are estimated by assigning them the shape and composition uncertainties of the prediction described in Sec. 5.5. They are allowed to float between $\frac{1}{1+U}$ and $1+U$ following a log-normal distribution, where U is the uncertainty of the corresponding nuisance parameter. I define the first bin of both contributions, which corresponds to the control region, to have a zero uncertainty. Therefore, nuisance parameters of the first bin, R_{τ}^1 and R_{ll}^1 , do not exist. Tab. 6.1 shows the uncertainties using the defined signal binning and their distributions.

Table 6.1.: Uncertainties of the nuisance parameters before they are injected into the MLL fit and their distributions (logN = log-normal distribution, logU = log-uniform distribution).

nuisance parameter R	R_{bg}	R_{ll}^2	R_{ll}^3	R_{ll}^4	R_{ll}^5	R_{ll}^6
rel. uncertainty U	100%	7.8%	11.8%	22.2%	37.5%	66.2%
distribution	logU	logN	logN	logN	logN	logN
nuisance parameter R	$R_{\tau,ll}$	R_{τ}^2	R_{τ}^3	R_{τ}^4	R_{τ}^5	R_{τ}^6
rel.uncertainty U	100%	3.8%	5.5%	8.6%	15.1%	26.0%
distribution	logU	logN	logN	logN	logN	logN

6.1.3. The Likelihood Function

The fit is done twice, once for the background-only model, and another time for the background-plus-signal model. The signal strength modifier r is the nuisance parameter of the signal, which is set to zero in the first case. Therefore, the likelihood function $L(data|r, \mathbf{R})$, which is maximized in order to obtain the nuisance parameters, looks as follows for both cases:

$$L(data|r, \mathbf{R}) = \prod_i \frac{1}{n^i!} E(r, \mathbf{R})^{n^i} e^{-E(r, \mathbf{R})}, \quad (6.2)$$

where E is the expectation value of the poisson distribution given by

$$E(r, \mathbf{R}) = r s^i + b^i(\mathbf{R}), \quad (6.3)$$

and each of the bins i is following a poisson distribution, s_i are the expected signals and $b^i(\mathbf{R})$ is the background model dependent on the nuisance parameters. The maxima of the likelihood function are found by minimizing the negative log-likelihood function using MINUIT [37].

6.1.4. Fit Results

Figure 6.1 (a) displays the terms that are injected into the MLL fit, whereas Fig. 6.1 (b) displays the quantities after the nuisance parameters are retrieved from the fit and applied as normalizations. The signal hypothesis in this figure is taken from the decoupled stop scenario in a gluino mass bin of 800 GeV and in a neutralino mass bin of 0 GeV. Both figures are shown for a selection of $\cancel{E}_T \geq 150$ GeV, $H_T \geq 400$ GeV, $n_{jets} \geq 4$ and $n_{btags} \geq 1$. The resulting nuisance parameters for this selection, as well as an $n_{jets} \geq 6$ selection are listed in table 6.2. The corresponding covariance matrices appear as shown in Tab. 6.3 for the 4 jets case, as well as in Tab. 6.5 for the 6 jets case. The corresponding correlation matrices can be found in Tab. 6.4 for the 4 jets case and in Tab. 6.6 for the 6 jets case.

Table 6.2.: Fit results for the normalization parameters for $\cancel{E}_T \geq 150$ GeV, $H_T \geq 400$ GeV and $n_{btags} \geq 1$. One row showing the results for $n_{jets} \geq 4$, another row showing results for $n_{jets} \geq 6$. The fit for $n_{jets} \geq 6$ was done using 5 instead of 6 bins. Their variances and covariances and correlations are shown in Tab. 6.3 and Tab. 6.4 for the 4 jets case and in Tab. 6.5 and Tab. 6.6 for the 6 jets case.

parameter	R_{bg}	$R_{ll,2}$	$R_{ll,3}$	$R_{ll,4}$	$R_{ll,5}$	$R_{ll,6}$
fit result (≥ 4 jets)	0.956	1.732	0.951	0.244	0.176	0.891
fit result (≥ 6 jets)	0.743	1.138	0.936	1.069	0.770	—
parameter	$R_{\tau,ll}$	$R_{\tau,2}$	$R_{\tau,3}$	$R_{\tau,4}$	$R_{\tau,5}$	$R_{\tau,6}$
fit result (≥ 4 jets)	1.013	1.516	0.960	0.400	0.122	0.924
fit result (≥ 6 jets)	1.797	1.095	0.920	1.213	0.550	—

The red error band in Fig. 6.1 (b) was calculated using a sampling method. A multivariate Gauss distribution is defined using the mean values of R-factors and the covariances obtained from the fit. A random sample of generated R-factors is taken following this multivariate Gauss distribution and the yields according to the defined model are calculated. After taking a sufficient number of random samples (1000), errors can be calculated for each bin. Since the values of the 84.1% quantile ($m + 1\sigma$) $x_{+\sigma}$ and the 15.9% quantile ($m - 1\sigma$) $x_{-\sigma}$ computed from these 1000 samples are, in general, assymmetric with respect to the median m , they are symmetrized by

$$\epsilon^i = \frac{x_{+\sigma}^i - x_{-\sigma}^i}{2} \quad (6.4)$$

In Tab. 6.7 and Tab. 6.8 one can see the observations and the background yields for

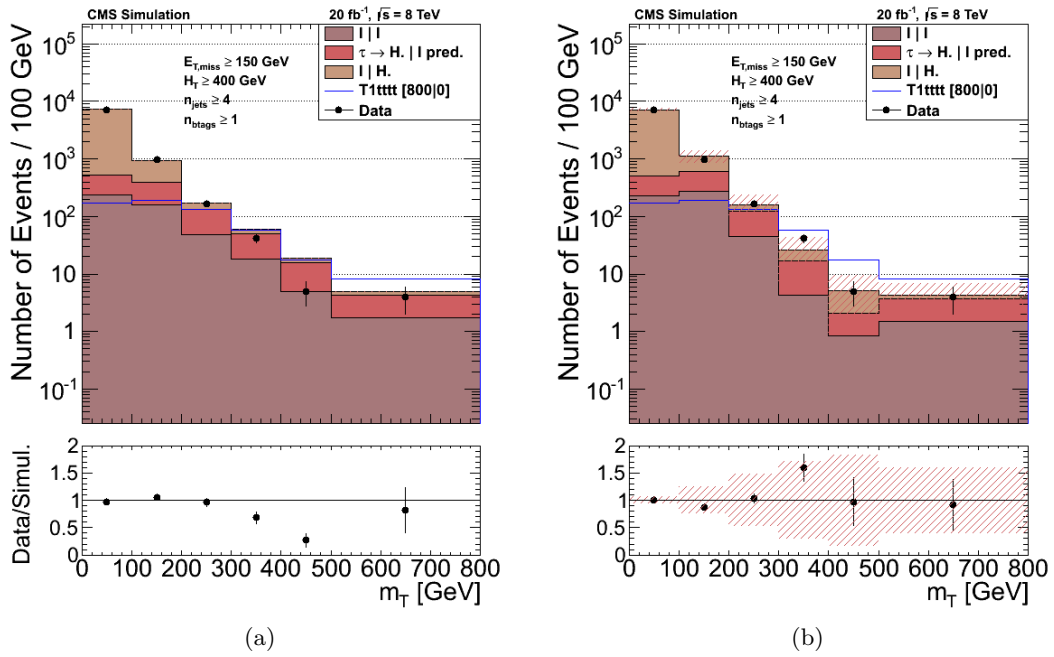


Figure 6.1.: Fit results for the $E_T \geq 150 \text{ GeV}$, $H_T \geq 400 \text{ GeV}$, $n_{jets} \geq 4$ and $n_{btags} \geq 1$ bin using a signal hypothesis of a gluino mass bin of 800 GeV and a neutralino mass bin of 0 GeV within the decoupled stop scenario. The number of m_T bins may vary provided that, each bin used in the analysis must contain all, an observation, a background hypothesis and a signal hypothesis. The fit in this case is done in 5 bins of 100 GeV and the last bin containing events in an m_T range of $[500, \infty]$. (a) Background prediction, observation and signal hypothesis as they are injected into the fit procedure. (b) Normalized background prediction with normalizations obtained from the fit, observation and signal hypothesis. The systematic errors of the background model obtained from the fit are striped in red.

Table 6.3.: Covariances of the fit parameters for $E_T \geq 150$ GeV, $H_T \geq 400$ GeV, $n_{jets} \geq 4$ and $n_{btags} \geq 1$.

	$R_{b\bar{b}}$	R_{ll}^2	R_{ll}^3	R_{ll}^4	R_{ll}^5	R_{ll}^6	$R_{tau,\mu}$	R_{τ}^2	R_{τ}^3	R_{τ}^4	R_{τ}^5	R_{τ}^6	
$R_{b\bar{b}}$	2.4 · 10 ⁻³	9 · 10 ⁻⁴	1.6 · 10 ⁻³	1 · 10 ⁻³	5 · 10 ⁻⁴	3 · 10 ⁻⁴	-8 · 10 ⁻⁴	-8 · 10 ⁻⁴	6 · 10 ⁻⁴	1.3 · 10 ⁻³	9 · 10 ⁻⁴	5 · 10 ⁻⁴	2 · 10 ⁻⁴
R_{τ}^2	9 · 10 ⁻⁴	0.9536	8 · 10 ⁻³	3.1 · 10 ⁻²	1.35 · 10 ⁻²	9.1 · 10 ⁻³	-1.83 · 10 ⁻²	-6.29 · 10 ⁻²	4.11 · 10 ⁻²	2.69 · 10 ⁻²	1.62 · 10 ⁻²	6.6 · 10 ⁻³	6.6 · 10 ⁻³
R_{ll}^2	1.6 · 10 ⁻³	8 · 10 ⁻³	0.8988	2.79 · 10 ⁻²	1.22 · 10 ⁻²	8.2 · 10 ⁻³	-7 · 10 ⁻³	-6.86 · 10 ⁻²	2.26 · 10 ⁻²	2.42 · 10 ⁻²	1.46 · 10 ⁻²	5.9 · 10 ⁻³	5.9 · 10 ⁻³
R_{ll}^3	1 · 10 ⁻³	3.1 · 10 ⁻²	2.79 · 10 ⁻²	0.7932	7.5 · 10 ⁻³	5 · 10 ⁻³	-7 · 10 ⁻³	-5.7 · 10 ⁻²	2.26 · 10 ⁻²	2.42 · 10 ⁻²	1.46 · 10 ⁻²	5.9 · 10 ⁻³	5.9 · 10 ⁻³
R_{ll}^4	5 · 10 ⁻⁴	1.35 · 10 ⁻²	1.22 · 10 ⁻²	7.5 · 10 ⁻³	0.7698	2.2 · 10 ⁻³	-4.7 · 10 ⁻³	-4.7 · 10 ⁻³	6.2 · 10 ⁻³	6.2 · 10 ⁻³	6.2 · 10 ⁻³	6.2 · 10 ⁻³	6.2 · 10 ⁻³
R_{ll}^5	3 · 10 ⁻⁴	9.1 · 10 ⁻³	8.2 · 10 ⁻³	5 · 10 ⁻³	2.2 · 10 ⁻³	0.8468	-3.2 · 10 ⁻³	-3.2 · 10 ⁻³	6.2 · 10 ⁻³	6.2 · 10 ⁻³	6.2 · 10 ⁻³	6.2 · 10 ⁻³	6.2 · 10 ⁻³
R_{ll}^6	3 · 10 ⁻⁴	9.1 · 10 ⁻³	8.2 · 10 ⁻³	5 · 10 ⁻³	2.2 · 10 ⁻³	0.8468	-3.2 · 10 ⁻³	-3.2 · 10 ⁻³	6.2 · 10 ⁻³	6.2 · 10 ⁻³	6.2 · 10 ⁻³	6.2 · 10 ⁻³	6.2 · 10 ⁻³
$R_{\tau, ll}$	-8 · 10 ⁻⁴	-1.83 · 10 ⁻²	-1.73 · 10 ⁻²	-7 · 10 ⁻³	-4.7 · 10 ⁻³	-3.2 · 10 ⁻³	6.9 · 10 ⁻³	-1.24 · 10 ⁻²	0.9657	2.79 · 10 ⁻²	1.83 · 10 ⁻²	1.18 · 10 ⁻²	4.8 · 10 ⁻³
R_{τ}^2	6 · 10 ⁻⁴	-6.29 · 10 ⁻²	3.44 · 10 ⁻²	2.1 · 10 ⁻²	9.2 · 10 ⁻³	6.2 · 10 ⁻³	-1.24 · 10 ⁻²	-1.24 · 10 ⁻²	0.9657	2.79 · 10 ⁻²	1.83 · 10 ⁻²	1.18 · 10 ⁻²	4.8 · 10 ⁻³
R_{τ}^3	1.3 · 10 ⁻³	4.11 · 10 ⁻²	-6.86 · 10 ⁻²	2.26 · 10 ⁻²	9.9 · 10 ⁻³	6.6 · 10 ⁻³	-1.4 · 10 ⁻²	-1.4 · 10 ⁻²	0.9313	1.96 · 10 ⁻²	1.18 · 10 ⁻²	4.8 · 10 ⁻³	4.8 · 10 ⁻³
R_{τ}^4	9 · 10 ⁻⁴	2.69 · 10 ⁻²	2.42 · 10 ⁻²	-5.7 · 10 ⁻²	6.5 · 10 ⁻³	4.4 · 10 ⁻³	-9.3 · 10 ⁻³	-9.3 · 10 ⁻³	1.83 · 10 ⁻²	1.96 · 10 ⁻²	1.18 · 10 ⁻²	4.8 · 10 ⁻³	4.8 · 10 ⁻³
R_{τ}^5	5 · 10 ⁻⁴	1.62 · 10 ⁻²	1.46 · 10 ⁻²	9 · 10 ⁻³	-1.61 · 10 ⁻²	2.6 · 10 ⁻³	-5.6 · 10 ⁻³	-5.6 · 10 ⁻³	1.1 · 10 ⁻²	1.18 · 10 ⁻²	7.8 · 10 ⁻³	0.8611	1.9 · 10 ⁻³
R_{τ}^6	2 · 10 ⁻⁴	6.6 · 10 ⁻³	5.9 · 10 ⁻³	3.6 · 10 ⁻³	1.6 · 10 ⁻³	-6.52 · 10 ⁻²	-2.3 · 10 ⁻³	-2.3 · 10 ⁻³	4.5 · 10 ⁻³	4.8 · 10 ⁻³	3.2 · 10 ⁻³	1.9 · 10 ⁻³	0.9247

Table 6.4.: Correlations of the fit parameters for $E_T \geq 150$ GeV, $H_T \geq 400$ GeV, $n_{jets} \geq 4$ and $n_{btags} \geq 1$.

	$R_{b\bar{b}}$	R_{ll}^2	R_{ll}^3	R_{ll}^4	R_{ll}^5	R_{ll}^6	$R_{tau,\mu}$	R_{τ}^2	R_{τ}^3	R_{τ}^4	R_{τ}^5	R_{τ}^6
$R_{b\bar{b}}$	1.0	1.81 · 10 ⁻²	3.36 · 10 ⁻²	2.31 · 10 ⁻²	5 · 10 ⁻³	6.6 · 10 ⁻³	-6.5 · 10 ⁻²	1.21 · 10 ⁻²	2.67 · 10 ⁻²	1.88 · 10 ⁻²	1.19 · 10 ⁻²	4.6 · 10 ⁻³
R_{τ}^2	1.81 · 10 ⁻²	1.0	5.51 · 10 ⁻²	3.58 · 10 ⁻²	1.58 · 10 ⁻²	2 · 10 ⁻³	-0.2253	-6.57 · 10 ⁻²	4.37 · 10 ⁻²	2.93 · 10 ⁻²	1.79 · 10 ⁻²	7 · 10 ⁻³
R_{ll}^2	3.36 · 10 ⁻²	5.51 · 10 ⁻²	1.0	3.31 · 10 ⁻²	1.47 · 10 ⁻²	9.4 · 10 ⁻³	-0.2198	3.7 · 10 ⁻²	-7.51 · 10 ⁻²	2.71 · 10 ⁻²	1.66 · 10 ⁻²	6.5 · 10 ⁻³
R_{ll}^3	2.31 · 10 ⁻²	3.58 · 10 ⁻²	3.31 · 10 ⁻²	1.0	9.6 · 10 ⁻³	6.2 · 10 ⁻³	-0.1446	2.4 · 10 ⁻²	2.63 · 10 ⁻²	-6.78 · 10 ⁻²	9 · 10 ⁻³	4.3 · 10 ⁻³
R_{ll}^4	5 · 10 ⁻³	1.58 · 10 ⁻²	1.47 · 10 ⁻²	9.6 · 10 ⁻³	1.0	2.7 · 10 ⁻³	-6.43 · 10 ⁻²	6 · 10 ⁻³	1.16 · 10 ⁻²	7.9 · 10 ⁻³	-1.98 · 10 ⁻²	1.9 · 10 ⁻³
R_{ll}^5	6.6 · 10 ⁻³	2 · 10 ⁻³	9.4 · 10 ⁻³	6.2 · 10 ⁻³	2.7 · 10 ⁻³	1.0	-4.12 · 10 ⁻²	6.8 · 10 ⁻³	7.5 · 10 ⁻³	5 · 10 ⁻³	3.1 · 10 ⁻³	-7.37 · 10 ⁻²
R_{ll}^6	-6.5 · 10 ⁻²	-0.2253	-0.2198	-0.1446	-6.43 · 10 ⁻²	-4.12 · 10 ⁻²	1.0	-0.1512	-0.1744	-0.1182	-7.28 · 10 ⁻²	-2.85 · 10 ⁻²
$R_{\tau, ll}$	1.21 · 10 ⁻²	-6.57 · 10 ⁻²	3.7 · 10 ⁻²	2.4 · 10 ⁻²	6 · 10 ⁻³	6.8 · 10 ⁻³	6.8 · 10 ⁻³	1.0	2.94 · 10 ⁻²	1.97 · 10 ⁻²	1.2 · 10 ⁻²	4.7 · 10 ⁻³
R_{τ}^2	1.21 · 10 ⁻²	-6.57 · 10 ⁻²	3.7 · 10 ⁻²	2.4 · 10 ⁻²	6 · 10 ⁻³	6.8 · 10 ⁻³	6.8 · 10 ⁻³	1.0	2.94 · 10 ⁻²	1.97 · 10 ⁻²	1.2 · 10 ⁻²	4.7 · 10 ⁻³
R_{τ}^3	2.67 · 10 ⁻²	4.37 · 10 ⁻²	-7.51 · 10 ⁻²	2.63 · 10 ⁻²	1.16 · 10 ⁻²	7.5 · 10 ⁻³	-0.1512	-0.1512	2.94 · 10 ⁻²	1.97 · 10 ⁻²	1.32 · 10 ⁻²	5.2 · 10 ⁻³
R_{τ}^4	1.88 · 10 ⁻²	2.93 · 10 ⁻²	2.71 · 10 ⁻²	-6.78 · 10 ⁻²	7.9 · 10 ⁻³	5 · 10 ⁻³	-0.1182	-0.1182	1.97 · 10 ⁻²	1.32 · 10 ⁻²	8.9 · 10 ⁻³	3.5 · 10 ⁻³
R_{τ}^5	1.19 · 10 ⁻²	1.79 · 10 ⁻²	1.66 · 10 ⁻²	9 · 10 ⁻³	-1.98 · 10 ⁻²	1.9 · 10 ⁻³	7.9 · 10 ⁻³	7.9 · 10 ⁻³	1.0	8.9 · 10 ⁻³	1.0	2.1 · 10 ⁻³
R_{τ}^6	4.6 · 10 ⁻³	7 · 10 ⁻³	6.5 · 10 ⁻³	4.3 · 10 ⁻³	1.9 · 10 ⁻³	-7.37 · 10 ⁻²	-2.85 · 10 ⁻²	-2.85 · 10 ⁻²	4.7 · 10 ⁻³	5.2 · 10 ⁻³	2.1 · 10 ⁻³	1.0

Table 6.5.: Covariances of the fit parameters for $\cancel{E}_T \geq 150$ GeV, $H_T \geq 400$ GeV, $n_{jets} \geq 6$ and $n_{btags} \geq 1$.

	R_{bg}^{b5}	R_{ll}^{l2}	R_{ll}^{l3}	R_{ll}^{l4}	R_{ll}^{l5}	$R_{tau, ll}$	$R_{\tau}^{\tau2}$	$R_{\tau}^{\tau3}$	$R_{\tau}^{\tau4}$	$R_{\tau}^{\tau5}$
R_{bg}^{b2}	$7.3 \cdot 10^{-3}$	$4.9 \cdot 10^{-3}$	$6.8 \cdot 10^{-3}$	$1.2 \cdot 10^{-3}$	$1.5 \cdot 10^{-3}$	$-1.13 \cdot 10^{-2}$	$3.4 \cdot 10^{-3}$	$8.6 \cdot 10^{-3}$	$3.6 \cdot 10^{-3}$	$2.9 \cdot 10^{-3}$
R_{ll}^{l2}	$4.9 \cdot 10^{-3}$	0.9162	$5.45 \cdot 10^{-2}$	$9.4 \cdot 10^{-3}$	$1.14 \cdot 10^{-2}$	$-6.47 \cdot 10^{-2}$	$-6.77 \cdot 10^{-2}$	$6.93 \cdot 10^{-2}$	$2.91 \cdot 10^{-2}$	$2.27 \cdot 10^{-2}$
R_{ll}^{l3}	$6.8 \cdot 10^{-3}$	$5.45 \cdot 10^{-2}$	0.9128	$7.5 \cdot 10^{-3}$	$9.3 \cdot 10^{-3}$	$-5.53 \cdot 10^{-2}$	$3.73 \cdot 10^{-2}$	$-7.31 \cdot 10^{-2}$	$2.34 \cdot 10^{-2}$	$1.84 \cdot 10^{-2}$
R_{ll}^{l4}	$1.2 \cdot 10^{-3}$	$9.4 \cdot 10^{-3}$	$7.5 \cdot 10^{-3}$	$9.8 \cdot 10^{-2}$	$1.6 \cdot 10^{-3}$	$-9.5 \cdot 10^{-3}$	$6.4 \cdot 10^{-3}$	$9.6 \cdot 10^{-3}$	$-5.36 \cdot 10^{-2}$	$3.2 \cdot 10^{-3}$
R_{ll}^{l5}	$1.5 \cdot 10^{-3}$	$1.14 \cdot 10^{-2}$	$9.3 \cdot 10^{-3}$	$1.6 \cdot 10^{-3}$	$2 \cdot 10^{-2}$	$-1.17 \cdot 10^{-2}$	$7.8 \cdot 10^{-3}$	$1.18 \cdot 10^{-2}$	$4.9 \cdot 10^{-3}$	$-1.55 \cdot 10^{-2}$
$R_{\tau, ll}$	$-1.13 \cdot 10^{-2}$	$-6.47 \cdot 10^{-2}$	$-5.53 \cdot 10^{-2}$	$-9.5 \cdot 10^{-3}$	$-1.17 \cdot 10^{-2}$	$7.27 \cdot 10^{-2}$	$-4.42 \cdot 10^{-2}$	$-2 \cdot 10^{-3}$	$-2.94 \cdot 10^{-2}$	$-2.32 \cdot 10^{-2}$
$R_{\tau}^{\tau2}$	$3.4 \cdot 10^{-3}$	$-6.77 \cdot 10^{-2}$	$3.73 \cdot 10^{-2}$	$6.4 \cdot 10^{-3}$	$7.8 \cdot 10^{-3}$	$-4.42 \cdot 10^{-2}$	0.9524	$4.74 \cdot 10^{-2}$	$1.99 \cdot 10^{-2}$	$1.55 \cdot 10^{-2}$
$R_{\tau}^{\tau3}$	$8.6 \cdot 10^{-3}$	$6.93 \cdot 10^{-2}$	$-7.31 \cdot 10^{-2}$	$9.6 \cdot 10^{-3}$	$1.18 \cdot 10^{-2}$	$-2 \cdot 10^{-3}$	$4.74 \cdot 10^{-2}$	0.8849	$2.97 \cdot 10^{-2}$	$2.33 \cdot 10^{-2}$
$R_{\tau}^{\tau4}$	$3.6 \cdot 10^{-3}$	$2.91 \cdot 10^{-2}$	$2.34 \cdot 10^{-2}$	$-5.36 \cdot 10^{-2}$	$4.9 \cdot 10^{-3}$	$-2.94 \cdot 10^{-2}$	$1.99 \cdot 10^{-2}$	$2.97 \cdot 10^{-2}$	0.8711	$9.8 \cdot 10^{-3}$
$R_{\tau}^{\tau5}$	$2.9 \cdot 10^{-3}$	$2.27 \cdot 10^{-2}$	$1.84 \cdot 10^{-2}$	$3.2 \cdot 10^{-3}$	$-1.55 \cdot 10^{-2}$	$-2.32 \cdot 10^{-2}$	$1.55 \cdot 10^{-2}$	$2.33 \cdot 10^{-2}$	$9.8 \cdot 10^{-3}$	0.8364

 Table 6.6.: Correlations of the fit parameters for $\cancel{E}_T \geq 150$ GeV, $H_T \geq 400$ GeV, $n_{jets} \geq 6$ and $n_{btags} \geq 1$.

	R_{bg}^{b2}	R_{ll}^{l2}	R_{ll}^{l3}	R_{ll}^{l4}	R_{ll}^{l5}	$R_{tau, ll}$	$R_{\tau}^{\tau2}$	$R_{\tau}^{\tau3}$	$R_{\tau}^{\tau4}$	$R_{\tau}^{\tau5}$
R_{bg}^{b2}	1.0									
R_{ll}^{l2}	$6 \cdot 10^{-2}$	1.0								
R_{ll}^{l3}	$8.29 \cdot 10^{-2}$	$5.95 \cdot 10^{-2}$	1.0							
R_{ll}^{l4}	$1.34 \cdot 10^{-2}$	$9.7 \cdot 10^{-3}$	$7.9 \cdot 10^{-3}$	1.0						
R_{ll}^{l5}	$1.87 \cdot 10^{-2}$	$1.29 \cdot 10^{-2}$	$5 \cdot 10^{-3}$	$1.7 \cdot 10^{-3}$	1.0					
$R_{\tau, ll}$	-0.4896	$-2 \cdot 10^{-2}$	-0.2144	$1.7 \cdot 10^{-3}$	$-4.69 \cdot 10^{-2}$	1.0				
$R_{\tau}^{\tau2}$	$3 \cdot 10^{-3}$	$-7.24 \cdot 10^{-2}$	$4 \cdot 10^{-2}$	$-3.5 \cdot 10^{-2}$	-0.168	1.0				
$R_{\tau}^{\tau3}$	$7 \cdot 10^{-2}$	$7.68 \cdot 10^{-2}$	$-8.13 \cdot 10^{-2}$	$1 \cdot 10^{-3}$	$5.16 \cdot 10^{-2}$	-0.2769	1.0			
$R_{\tau}^{\tau4}$	$4.48 \cdot 10^{-2}$	$3.25 \cdot 10^{-2}$	$2.62 \cdot 10^{-2}$	$-5.72 \cdot 10^{-2}$	$2.18 \cdot 10^{-2}$	-0.1167	1.0			
$R_{\tau}^{\tau5}$	$3.75 \cdot 10^{-2}$	$2.59 \cdot 10^{-2}$	$2.1 \cdot 10^{-2}$	$-1.82 \cdot 10^{-2}$	$1.74 \cdot 10^{-2}$	$1.14 \cdot 10^{-2}$	1.0			

each bin after the normalizations are obtained from the MLL fit.

Table 6.7.: Data compared to predicted background for $\cancel{E}_T \geq 150$ GeV, $H_T \geq 400$ GeV, $n_{jets} \geq 4$, and $n_{btags} \geq 1$.

	control bin	bin 2	bin 3	bin 4	bin 5	bin 6
data	7171	975	163	41	5	4
bg	7098 ± 480	1127 ± 274	157.6 ± 75.2	25.7 ± 18.2	5.1 ± 4.2	4.3 ± 2.6

Table 6.8.: Data compared to predicted background for $\cancel{E}_T \geq 150$ GeV, $H_T \geq 400$ GeV, $n_{jets} \geq 6$ and $n_{btags} \geq 1$.

	control bin	bin 2	bin 3	bin 4	bin 5
data	1061	149	29	7	1
bg	947.3 ± 97.9	137.1 ± 37.9	25.8 ± 14.2	5.9 ± 3.3	1.9 ± 1.4

6.2. Limit Calculation

One approach of calculating an exclusion limit is the so-called CL_s method [38, 39]. It is a method to compare the compatibility of the data with the background-only and signal-plus-background hypotheses using the likelihood function $L(data|r, \mathbf{R})$ defined by Eq. (6.2).

6.2.1. Observed Limit

A test statistic is constructed based on the profile likelihood ratio:

$$q(r) = -2 \ln \frac{L(data|r, \hat{\mathbf{R}}_r)}{L(data|\hat{r}, \hat{\mathbf{R}})}, \quad (6.5)$$

where $\hat{\mathbf{R}}_r$ is the maximum likelihood estimator of \mathbf{R} for a given r . Furthermore, \hat{r} and $\hat{\mathbf{R}}$ are the maximum likelihood estimators of the global maximum. For a given signal strength modifier r , q_r^{obs} is the observed value of the test statistic, while $\hat{\mathbf{R}}_r^{obs}$ and $\hat{\mathbf{R}}_0^{obs}$ are the maximum likelihood estimators for the signal-plus-background and the background-only hypotheses, respectively. Then, probability density functions $f(q|r, \hat{\mathbf{R}}_r^{obs})$ and $f(q|0, \hat{\mathbf{R}}_0^{obs})$ are constructed by generating toys. Using these functions, the confidence levels of the background-only (CL_b) and the signal-plus-background hypotheses (CL_{s+b}) are defined:

$$CL_{s+b} = P(q \geq q_r^{obs} | s + b) = \int_{q_r^{obs}}^{\infty} f(q | r, \hat{\mathbf{R}}_r^{obs}) dq, \quad (6.6)$$

$$CL_b = P(q \geq q_r^{obs} | b) = \int_{q_0^{obs}}^{\infty} f(q | 0, \hat{\mathbf{R}}_0^{obs}) dq \quad (6.7)$$

These quantities are used to calculate the ratio

$$CL_s = \frac{CL_{s+b}}{CL_b}. \quad (6.8)$$

For $CL_s \leq \alpha$ and a given r , the signal hypothesis is excluded with a $(1 - \alpha)$ confidence level. The 95% confidence level upper limit on the signal strength modifier r is reached by adjusting r so that $CL_s = 0.05$. The 95% confidence level upper limit on the production cross sections is the hypothetical production cross section multiplied with the signal strength modifier at $CL_s = 0.05$. This limit is calculated for each point on the simplified models parameter planes for each simplified model used and can be seen in Fig. 6.2, Fig. 6.3 and Fig. 6.4. The observed exclusion line is drawn, where r takes the value 1¹.

6.2.2. Expected Limit

The expected limits correspond to the expected median upper limit of the signal strength modifier. They are calculated by generating a large set of background-only toys and calculating the CL_s and its 95% confidence level upper limit on r for each toy as if it were data, as described in the former section. The cumulative probability function of the results of the toys is built, whose quantiles (16%, 50%, 84%) correspond to the median and its $\pm 1\sigma$ band. Analogously to the observed limit, the exclusion lines for the expected limit and its $\pm 1\sigma$ band are drawn in Fig. 6.2, Fig. 6.3 and Fig. 6.4, where the evaluated signal strength modifier is 1 for $CL_s = 0.05$.

6.2.3. Resulting Exclusion Limits

No excess over the prediction and therefore no new physics has been found. The interpretation of the results is done in terms of exclusions using simplified models. The histogram in Fig. 6.2 shows the decoupled stop scenario exclusion limits on the cross section for the region $\cancel{E}_T \geq 150$ GeV, $H_T \geq 400$ GeV, $n_{jets} \geq 6$ and $n_{btags} \geq 1$. As a comparison the exclusion limits for two different methods are shown, one of which used

¹ $r > 1$ for $CL_s = 0.05$ means, that the signal yield must be r times larger in order to exclude the signal hypothesis. $r < 1$ for $CL_s = 0.05$ means, that even a signal, which is r times smaller, can be excluded.

$\Delta\phi$ (between the W boson and the single lepton) as the discriminating variable. This method is very similar to the m_T method and results in a high exclusion limit for the region $H_T > 500$ GeV, $n_{jets} \geq 6$ and $n_{btags} \geq 2$ and $\Delta\phi > 1$. The other method is based on selections on \cancel{E}_T and H_T and a prediction using \cancel{E}_T templates. Figure 6.3 shows the 95% confidence level upper limit on the cross sections of the frozen neutralino mass scenario, while Fig. 6.4 shows the same relation for the frozen gluino mass scenario. Again, the m_T prediction method is compared to the published \cancel{E}_T templates method for both models. It can be seen, that the exclusion lines of these two scenarios are not dependent on the stop mass at high stop quark masses, which is depicted by the decoupled stop scenario.

The higher the masses of the SUSY particles, the lower the production cross section. Therefore, high mass regions of the parameter planes are more difficult to exclude. We notice, that the published results have a higher mass exclusion limit than the ones obtained within this thesis. One reason is, that the published results calculate their exclusions using a higher b-tag requirement, $n_{btags} \geq 2$ or even $n_{btags} \geq 3$. Selections on high b-tag multiplicities increase the signal-to-background ratio significantly and therefore higher masses in the different parameter planes can be excluded. Regarding the methods of this thesis, there are not enough predicted events in high regions of m_T ($m_T \geq 400$ GeV) to fill bins for a higher b-tag multiplicity requirement than $n_{btags} \geq 1$. Since a signal yield, a background yield and an observation for each of the defined bins are mandatory, a limit cannot be calculated in this case.

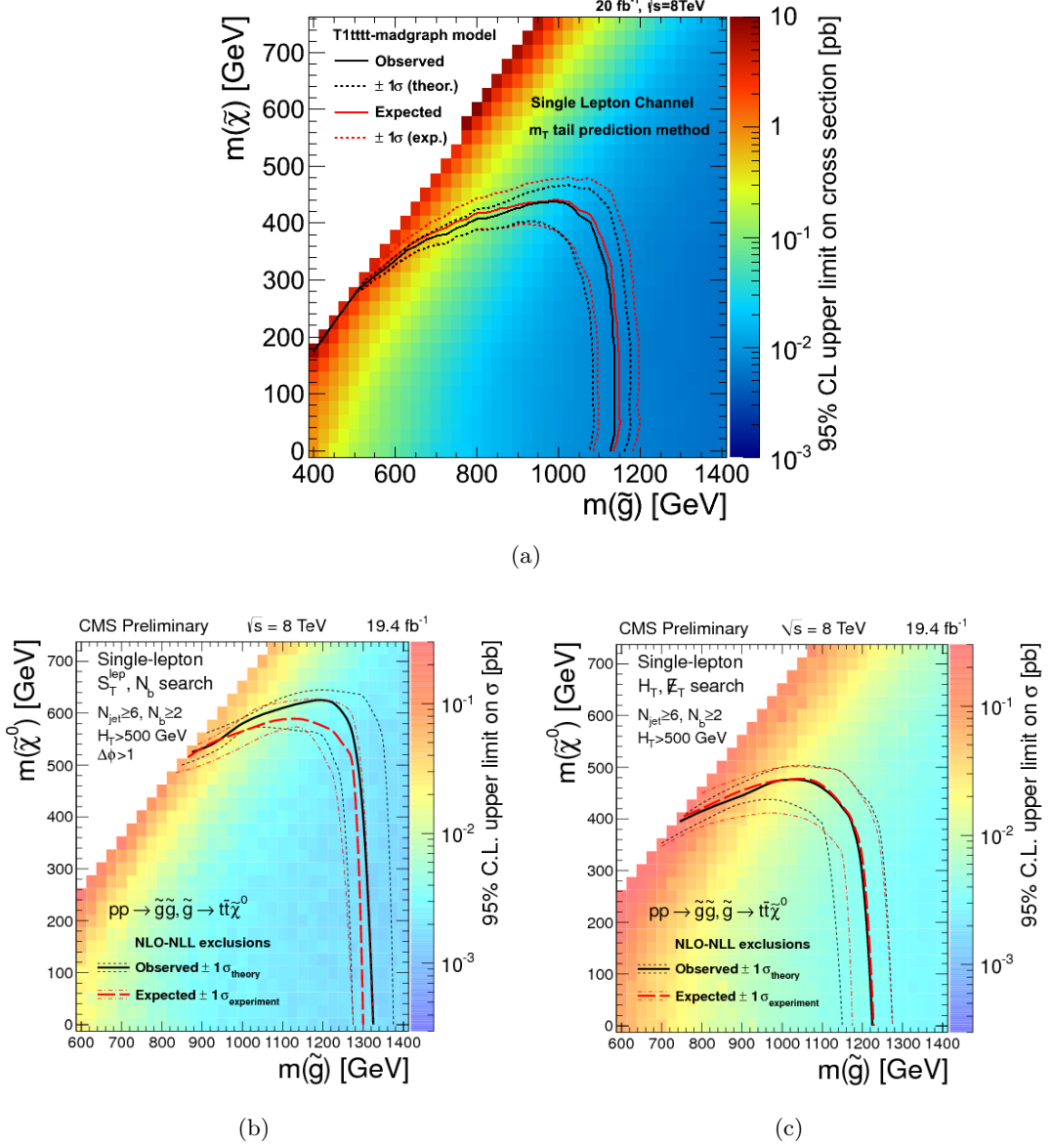


Figure 6.2.: (a) 95% confidence level upper limit on cross section and exclusion lines for the decoupled stop scenario in the single lepton channel utilizing the m_T tail prediction method as done within this thesis. The considered signal region that results in these exclusion limits is $\cancel{E}_T \geq 150 \text{ GeV}$, $H_T \geq 400 \text{ GeV}$, $n_{\text{jets}} \geq 6$ and $n_{\text{btags}} \geq 1$. (b) Exclusion histogram using the $\Delta\phi$ method [40]. (c) Exclusion limits using the \cancel{E}_T template method [40].

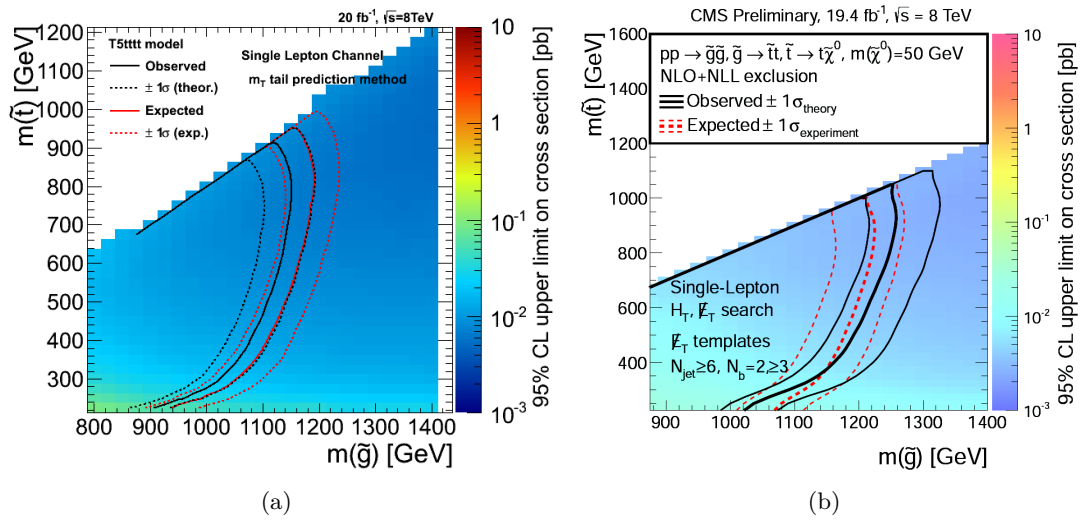


Figure 6.3.: (a) 95% confidence level upper limit on cross section and exclusion lines for the frozen neutralino mass scenario in the single lepton channel utilizing the m_T tail prediction method as done within this thesis. The considered signal region that results in these exclusion limits is $\cancel{E}_T \geq 150\text{ GeV}$, $H_T \geq 400\text{ GeV}$, $n_{jets} \geq 6$ and $n_{btags} \geq 1$. (b) Exclusion limits using the \cancel{E}_T template method [35].

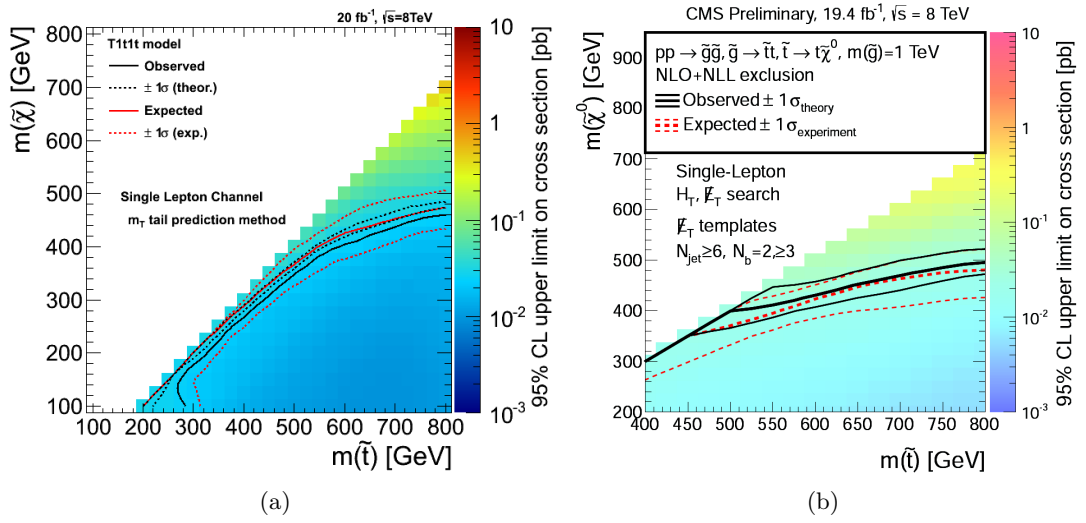


Figure 6.4.: (a) 95% confidence level upper limit on cross section and exclusion lines for the frozen gluino mass scenario in the single lepton channel utilizing the m_T tail prediction method as done within this thesis. The considered signal region that results in these exclusion limits is $\cancel{E}_T \geq 150\text{ GeV}$, $H_T \geq 400\text{ GeV}$, $n_{\text{jets}} \geq 6$ and $n_{\text{btags}} \geq 1$. (b) Exclusion limits using the \cancel{E}_T template method [35].

7. Summary and Outlook

Within this thesis, the distribution given by the transverse mass of the W boson applied on single leptonic events has been examined with a special focus on the tail of the distribution. It is important to understand the quantities and qualities of the different contributions in order to accomplish a prediction. Different attempts of m_T tail predictions have been done, of which two are described extensively in the previous chapters, the “correction method” and the “dilepton method”. The focus on this thesis was clearly on the development of methods for these predictions and on the performance of them. The tool used to calculate the limits and exclusion, as well as performing the fit, was developed to combine results of ATLAS and CMS analysis in order to find the Higgs boson, which made this part of the work, that some may consider the lion’s share, comparably fast and convenient.

The results show that the m_T variable is a good discriminator between the SM background and the expected SUSY signal and quite competitive, if some fine tuning is performed in all the steps this thesis guided through. This method and the transverse mass of the W boson as a discriminator will not be further applied on 2012 data, but are very promising techniques for future runs at the LHC, at higher luminosities and energies. The number of background events and expected signal events in m_T tail regions will be higher, which will allow us to utilize more selective b-tag requirements and therefore obtain higher signal-to-background ratios. This will increase the exclusion limits or lead to a discovery. At HEPHY, a novel multi-variate analysis (MVA) method is currently developed in order to enhance the sensitivity of CMS at difficult SUSY mass configurations. The transverse mass can be used as an input variable in common MVA methods such as neural networks or boosted decision trees. As a next step, the improvement in sensitivity caused by the m_T among other kinematic variables, needs to be studied in detail using these methods, before it is applied on new data of 14 TeV collisions in 2015. Furthermore, the discovery potential for the new data needs to be estimated.

Exciting and challenging times for particle physicists are ahead and we never know, how far away we are from a new discovery. May a day like the 4th of July 2012, when the discovery of a Higgs boson was announced, come rather sooner than later, also for the SUSY analysis groups.

Appendices

A. Datasets and Tables

A.1. Dataset Used for QCD Estimation

The QCD background estimation of Sec. 4.5 was partly done with hadronically triggered datasets, in order to avoid a I_{rel} bias from the EleHad samples. The datasets consist of events, that were triggered by different HLT_HT triggers. The lower the selection is, the lower must be the trigger requirement, which implies that the prescales as well as the statistical errors of the bins are higher. Since the QCD is almost vanishing in the used single lepton search selection, which has been shown within this estimation, these errors are acceptable. Using HLT_HT trigger, we have to keep its response curves in mind, e.g., a HLT_HT_300 trigger efficient not below a H_T value of ~ 350 GeV. Tab. A.1 shows the data sets used for this estimation.

Table A.1.: Data samples used QCD estimation

HT-Run2012A-13Jul2012
JetHT-Run2012B-13Jul2012
JetHT-Run2012C-Aug24ReReco
JetHT-Run2012C-PromptReco-v2
JetHT-Run2012D-PromptReco

A.2. Dataset Used for Dilepton Prediction

The dilepton prediction was done using dileptonic data sets. The utilized data sets are listed in Tab. A.2

Table A.2.: Data samples used for the dilepton prediction

$\mu + \mu$
DoubleMu-Run2012A-13Jul2012
DoubleMu-Run2012B-13Jul2012
DoubleMu-Run2012C-PromptReco
DoubleMu-Run2012C-PromptReco-v2
$e + e$
DoubleElectron-Run2012A-13Jul2012
DoubleElectron-Run2012B-13Jul2012
DoubleElectron-Run2012C-PromptReco
DoubleElectron-Run2012C-PromptReco-v2
$\mu + e$
MuEG-Run2012A-13Jul2012
MuEG-Run2012B-13Jul2012
MuEG-Run2012C-Aug24ReReco
MuEG-Run2012C-PromptReco-v2
MuEG-Run2012D-PromptReco

produces exactly these card files readable to the Higgs Combine Tool. The necessary information just needs to be transferred to the card file writer within a few methods.

List of Tables

1.1.	Particle content of the SM	1
1.2.	Particles and their superpartners in the unbroken MSSM	5
4.1.	Data samples used for analysis	25
4.2.	Additional requirements for well identified single lepton analysis muons and veto muons.	26
4.3.	Requirements for well identified single lepton analysis electrons and veto electrons.	27
4.4.	Estimation on the QCD contribution in the ≥ 1 b-tag bin. The low H_T electron signal region (marked with *) corresponds to the inclusive bin $250 < \cancel{E}_T < 2500$ GeV. The regions of H_T in the first line are given in GeV.	31
5.1.	Prediction for m_T tail of the hadronic tau contribution using correction templates for different signal regions. The table does not show the statistical uncertainties from MC.	41
5.2.	Prediction for m_T tail of the lost lepton contribution using correction templates for different signal regions. The table does not show the statistical uncertainties from MC.	42
5.3.	Prediction for the m_T tail of the hadronic tau contribution using dilepton events and different signal regions. The table does not show the statistical uncertainties from MC.	45
5.4.	Prediction for the m_T tail of the lost lepton contribution from dilepton events for different signal regions. The table does not show the statistical uncertainties from MC.	46
6.1.	Uncertainties of the nuisance parameters before they are injected into the MLL fit and their distributions (logN = log-normal distribution, logU = log-uniform distribution).	53

6.2. Fit results for the normalization parameters for $\cancel{E}_T \geq 150$ GeV, $H_T \geq 400$ GeV and $n_{btags} \geq 1$. One row showing the results for $n_{jets} \geq 4$, another row showing results for $n_{jets} \geq 6$. The fit for $n_{jets} \geq 6$ was done using 5 instead of 6 bins. Their variances and covariances and correlations are shown in Tab. 6.3 and Tab. 6.4 for the 4 jets case and in Tab. 6.5 and Tab. 6.6 for the 6 jets case.	54
6.3. Covariances of the fit parameters for $\cancel{E}_T \geq 150$ GeV, $H_T \geq 400$ GeV, $n_{jets} \geq 4$ and $n_{btags} \geq 1$	56
6.4. Correlations of the fit parameters for $\cancel{E}_T \geq 150$ GeV, $H_T \geq 400$ GeV, $n_{jets} \geq 4$ and $n_{btags} \geq 1$	56
6.5. Covariances of the fit parameters for $\cancel{E}_T \geq 150$ GeV, $H_T \geq 400$ GeV, $n_{jets} \geq 6$ and $n_{btags} \geq 1$	57
6.6. Correlations of the fit parameters for $\cancel{E}_T \geq 150$ GeV, $H_T \geq 400$ GeV, $n_{jets} \geq 6$ and $n_{btags} \geq 1$	57
6.7. Data compared to predicted background for $\cancel{E}_T \geq 150$ GeV, $H_T \geq 400$ GeV, $n_{jets} \geq 4$, and $n_{btags} \geq 1$	58
6.8. Data compared to predicted background for $\cancel{E}_T \geq 150$ GeV, $H_T \geq 400$ GeV, $n_{jets} \geq 6$ and $n_{btags} \geq 1$	58
A.1. Data samples used QCD estimation	69
A.2. Data samples used for the dilepton prediction	70

List of Figures

1.1.	Running coupling constants.	3
1.2.	(a) Fermion f coupling to a Higgs boson and (b) scalar coupling to a Higgs boson.	4
1.3.	The Feynman graphs of the utilized simplified models spectrum	7
2.1.	A scheme of the LHC accelerator complex with an overall view of the experiments [10]	9
3.1.	The Compact Muon Solenoid. A view of the transverse plane [19].	14
3.2.	Schematic view of the tracker, the ECAL, HCAL, HF, the magnet and the muon system [14].	15
3.3.	Architecture of the L1-Trigger [14].	17
4.1.	Distributions for single lepton preselections, showing observed data compared to standard model backgrounds obtained from simulations.	21
4.2.	Feynman diagrams of typical processes involved in $t\bar{t}$ pair production	24
4.3.	Control regions (C and D) for: (a) muons (b) electrons	28
4.4.	QCD background estimation using the ABCD method. Signal regions (A) and I_{rel} sidebands (B) as well as the normalized control shapes are shown	29
4.5.	Scheme of the ABCD method and its regions.	30
5.1.	The m_T distribution in the single lepton channel as obtained from simulation and compared to data.	34
5.2.	The $Lepton Lepton$ contribution	37
5.3.	The four major contributions to the m_T distribution	38
5.4.	Templates showing the correlation of m_T before (y -axis) and after (x -axis) the recalculation of \cancel{E}_T	39
5.5.	Prediction using correction templates	40
5.6.	Two tau templates used in the $\tau \rightarrow Hadrons Lepton$ prediction	43
5.7.	Prediction of the $\tau \rightarrow Hadrons Lepton$ distribution from dilepton events for a signal region.	44

5.8. Prediction of the $\tau \rightarrow Hadrons Lepton$ shape from dilepton events . . .	48
5.9. Prediction of the $Lepton Lepton$ distribution from dilepton events . . .	49
5.10. K-factors.	50
6.1. Fit results for the decoupled stop scenario	55
6.2. Decoupled stop scenario exclusion plot	61
6.3. Frozen neutralino mass scenario exclusion plot	62
6.4. Frozen gluino mass scenario exclusion plot	63
B.1. Part of a card file used as input for the Higgs Combine Tool	71

Bibliography

- [1] D.J. Griffiths (1987). *Introduction to Elementary Particles*. 1987.
- [2] S. Chatrchyan et al. Observation of a new boson at a mass of 125 GeV with the CMS experiment at the LHC. *Phys.Lett.*, B716:30–61, 2012.
- [3] F. Zwicky. Die Rotverschiebung von extragalaktischen Nebeln. *Helvetica Physica Acta*, 6:110–127, 1933.
- [4] Planck Collaboration, P. A. R. Ade, N. Aghanim, C. Armitage-Caplan, M. Arnaud, M. Ashdown, F. Atrio-Barandela, J. Aumont, C. Baccigalupi, A. J. Banday, and et al. Planck 2013 results. I. Overview of products and scientific results. *ArXiv e-prints*, March 2013.
- [5] H. Georgi and S. L. Glashow. Unity of All Elementary-Particle Forces. *Physical Review Letters*, 32:438–441, February 1974.
- [6] A. J. Buras, J. Ellis, M. K. Gaillard, and D. V. Nanopoulos. Aspects of the grand unification of strong, weak and electromagnetic interactions. *Nuclear Physics B*, 135:66–92, March 1978.
- [7] Stephen P. Martin. A Supersymmetry primer. *arXiv, hep-ph/9709356*, 1997.
- [8] A. Djouadi et al. The Minimal supersymmetric standard model: Group summary report. *arXiv, hep-ph/9901246*, 1998.
- [9] Daniele Alves et al. Simplified Models for LHC New Physics Searches. *J.Phys.*, G39:105005, 2012.
- [10] Jean-Luc Caron. Overall view of LHC experiments, 1998.
- [11] Lyndon Evans and Philip Bryant (editors). LHC Machine. *JINST*, 3:S08001, 2008.
- [12] Nicolò Cartiglia. Measurement of the proton-proton total cross section at 2, 7, 8 and 57 TeV. *arXiv, 1303.2927*, pages 55–64, 2013.
- [13] The TOTEM Collaboration. The TOTEM Experiment at the CERN Large Hadron Collider. *JINST*, 3:S08006, 2008.

- [14] S. Chatrchyan et al. The CMS experiment at the CERN LHC. *JINST*, 3:S08004, 2008.
- [15] The ATLAS Collaboration. The ATLAS Experiment at the CERN Large Hadron Collider. *JINST*, 3:S08003, 2008.
- [16] The ALICE Collaboration. The ALICE Experiment at the CERN LHC. *JINST*, 3:S08002, 2008.
- [17] The LHCb Collaboration. The LHCb Detector at the LHC. *JINST*, 3:S08005, 2008.
- [18] The LHCf Collaboration. The LHCf Detector at the CERN Large Hadron Collider. *JINST*, 3:S08006, 2008.
- [19] CMS. Transverse Slice of the Compact Muon Solenoid (CMS) Detector. <http://cms.web.cern.ch/news/how-cms-detects-particles/>, May 2013. Accessed: 2013-11-27.
- [20] The CMS Trigger and Data Acquisition Group. The cms high level trigger. *arXiv*, *hep-ex/0512077*, November 2005.
- [21] CMS Collaboration. Particle-Flow Event Reconstruction in CMS and Performance for Jets, Taus, and \cancel{E}_T . CMS Physics Analysis Summary CMS-PAS-PFT-09-001, 2009.
- [22] CMS Collaboration. Commissioning of the Particle-flow Event Reconstruction with the first LHC collisions recorded in the CMS detector. <http://cdsweb.cern.ch/record/1247373>, 2010.
- [23] Matteo Cacciari, Gavin P. Salam, and Gregory Soyez. The Anti-k(t) jet clustering algorithm. *JHEP*, 0804:063, 2008.
- [24] CMS Collaboration. Determination of the Jet Energy Scale in CMS with pp Collisions at $\sqrt{s} = 7$ TeV. <http://cdsweb.cern.ch/record/1308178>, 2010.
- [25] CMS Collaboration. Missing transverse energy performance of the CMS detector. *Journal of Instrumentation*, 6:9001, September 2011.
- [26] The CMS collaboration. Identification of b-quark jets with the CMS experiment. *arXiv*, *hep-ex/1211.4462v2*, 29 May 2013.
- [27] J. Beringer et al. (Particle Data Group). Particle Data Booklet. *Phys. Rev. D* 86, 010001, 2012.

- [28] J. Alwall et al. MadGraph5: going beyond. *JHEP*, doi:10.1007/JHEP06(2011)128, 06.
- [29] P. Nason S. Frixione and C. Oleari. Matching NLO QCD computations with Parton Shower simulations: the POWHEG method. *JHEP*, doi:10.1088/1126-6708/2007/11/070, 11.
- [30] S. Mrenna T. Söstrand and P. Z. Skands. PYTHIA 6.4 physics and manual. *JHEP*, doi:10.1088/1126-6708/2006/05/026, 05, 2006.
- [31] Z. Was. TAUOLA the library for tau lepton decay. *Nucl. Phys. Proc. Suppl.*, 98, 2001.
- [32] GEANT4 Collaboration. The fast simulation of the CMS detector at LHC. *Nucl. Instrum. Meth. A*, 506, 2003.
- [33] Performance of muon reconstruction and identification in pp collisions at $\sqrt{s} = 7$ TeV. Technical Report CMS-PAS-MUO-10-004, CERN, Geneva, 2011.
- [34] Electron reconstruction and identification at $\sqrt{s} = 7$ TeV. Technical Report CMS-PAS-EGM-10-004, CERN, Geneva, 2010.
- [35] W. Adam et al. Search for supersymmetry in the single lepton channel using hadronic observables and the 8 TeV dataset. *CMS-PAS-SUS-13-007*, 2013.
- [36] D Kovalskiy, M Tadel, A Mrak-Tadel, B Bellenot, V Kuznetsov, C D Jones, L Bauerdick, M Case, J Mülmenstadt, and A Yagil. Fireworks: A physics event display for cms. *Journal of Physics: Conference Series*, 219(3):032014, 2010.
- [37] F James and M Roos. MINUIT: a system for function minimization and analysis of the parameter errors and corrections. *Comput. Phys. Commun.*, 10(CERN-DD-75-20):343–367. 38 p, Jul 1975.
- [38] G. Cowan, K. Cranmer, E. Gross, and O. Vitells. Asymptotic formulae for likelihood-based tests of new physics. *European Physical Journal C*, 71:1554, February 2011.
- [39] Mingshui Chen A. Korytov, Giovanni Petrucciani et. al. Procedure for the LHC Higgs boson search combination in summer 2011. *CMS AN -2011/29*, 2011.
- [40] The CMS Collaboration. Search for Supersymmetry in pp collisions at 8 TeV in events with a single lepton, multiple jets and b-tags. *CMS-PAS-SUS-13-007*, 2013.